Journal of Theoretical Biology 432 (2017) 55–79

Contents lists available at ScienceDirect

Journal of Theoretical Biology

journal homepage: www.elsevier.com/locate/jtbi

A time-space model for the growth of microalgae biofilms for biofuel production

B. Polizzi[a], O. Bernard[b,c], M. Ribot[d,*]

[a] Institut de Mécanique des Fluides de Toulouse, CNRS UMR 5502, France
[b] Inria, Sophia Antipolis Méditerranée Research Centre, Project BIOCORE, France
[c] LOV-UPMC-CNRS, UMR 7093, Station Zoologique, Villefranche-sur-mer, France
[d] Université d'Orléans, CNRS, MAPMO, UMR CNRS 7349, rue de Chartres, BP 6759, F-45067 Orléans Cedex 2, France

ARTICLE INFO

Article history:
Received 4 December 2016
Revised 17 March 2017
Accepted 17 August 2017
Available online 18 August 2017

Keywords:
Biofilm growth
Photosynthetic microalgae biofilm
Front propagation
Fluid dynamics model
Numerical simulations

ABSTRACT

We present in this paper a spatial model describing the growth of a photosynthetic microalgae biofilm. In this model we consider photosynthesis, extracellular matrix excretion, and mortality. These mechanisms are described precisely using kinetic laws that take into account some saturation effects which limit the reaction rates and involve different components that we treat individually. In particular, to obtain a more detailed description of the microalgae growth, we consider separately the lipids they contain and the functional part of microalgae (proteins, RNA, etc ...), the latter playing a leading role in photosynthesis. We also consider the components dissolved in liquid phase as CO_2. The model is based on mixture theory and the behaviour of each component is described on the one hand by mass conservation, which takes into account biological features of the system, and on the other hand by conservation of momentum, which describes the physical properties of the components. Some numerical simulations are displayed in the one-dimensional case and show that the model is able to estimate accurately the biofilm productivity.

1. Introduction

The term "biofilm" was introduced by Costerton et al. (1978) in 1978 to design a mixture of organisms, embedded in an extracellular matrix and attached to a surface in contact with water. The extra-cellular matrix (ECM) gathers all the extracellular molecules secreted by micro-organisms together with dead cells. The ECM provides structural and biochemical support to the surrounding micro-organisms. Biofilm is the prevailing mode of micro-organisms life. They are ubiquitous in nature and they appear commonly in various domains, such as medical infections, reprocessing of waste or production of clean energy.

The formation of a biofilm follows well-identified steps. At the beginning, micro-organisms colonise the surface, then the colony grows and organises within an extra-cellular matrix and finally some of the organisms are dispersed in order to colonise another location of the surface. The extra-cellular matrix plays a particular role in this organisation, since it acts as a barrier and provides a protection for the whole colony. However, the physical structure of a biofilm, which has a gel-like structure, is still unclear: in the same biofilm, some fractions have a viscous behaviour, whereas other fractions have a visco-elastic structure (Galy et al., 2012). Moreover, even if the biofilm contains liquid inside, it is mainly in a solid phase.

During the last decades, the study of microalgae biofilm has become an important field of research. Although microalgae biofilms are almost always detrimental in industrial fields (Kjellerup et al., 2009), it is a credible alternative for the production of clean energy, which is one of the biggest challenge of our century.

Indeed, there exist a wide variety of microalgae species that are able to develop as a biofilm and to produce chemical components for green chemistry production, including biofuel production (Wijffels and Barbosa, 2010). The main interest of a biofilm culture, in comparison with usual cultures of microalgae in suspension, is the reduction of the harvesting cost. Indeed, it is estimated that the biomass obtained from biofilm contains between 80% and 90% of water instead of more than 99% for cultures in suspension (Gross et al., 2013). Moreover, for a classical microalgae culture in suspension, several steps are needed to remove the water and to concentrate the products, which is both time consuming and expensive. On the opposite, for a biofilm system, microalgae are stuck on a surface and are harvested by scraping.

The comprehension of the development of biofilms is an important topic of research. It has motivated the introduction of several

* Corresponding author.
E-mail addresses: bastien.polizzi@imft.fr (B. Polizzi), olivier.bernard@inria.fr (O. Bernard), magali.ribot@univ-orleans.fr (M. Ribot).

http://dx.doi.org/10.1016/j.jtbi.2017.08.017
0022-5193/

mathematical models to understand better the main mechanisms driving the biofilm growth and structuration. For an overview of mathematical models for biofilms in general, see Horn and Lackner (2014); Wang and Zhang (2010). The first class of models are based on ordinary differential equations (ODE) (Wolf et al., 2007) and take into account the kinetic reactions involved in the biofilm growth. These models rely on a precise description of metabolic reactions by considering many components and using a detailed modelling of the mass transfers between components

A second type of models are multidimensional and multispecies cell centered models (van Loosdrecht et al., 2002). The solutions of these discrete models are obtained by individual based approaches or cellular automata. In these models also, many biological features are included thanks to the precise description of the mechanisms. However, fluid mechanics effects are difficult to take into account and, despite the recent advances in parallel computing that enable to simulate the evolution of a few hundreds of cells, this approach remains quite expensive from a computational perspective. Thus, hybrid models, coupling some cell-centered approaches with partial differential equations, have been proposed to improve this point (Alpkvist et al., 2006).

A third approach represents biofilms with fully continuous models based on partial differential equations (PDE). In such models, the biofilm is described as a viscoelastic material that expands in response to the pressure induced by mass exchanges between the biofilm and the surrounding liquid. Several strategies can be used to describe the spatial structure of biofilms : in some PDE models, biofilm and liquid are separated by a physical interface, the evolution of which is computed by moving front techniques (Alpkvist and Klapper, 2007; Dockery and Klapper, 2001/02). Another modelling strategy relies on mixture theory, which does not require to represent the evolution of an interface. Mixture theory was introduced in the 1960s by a series of articles by Trusdell and provides continuous models based on PDEs for multi-component fluids by assuming that several components may be present locally; for more details about mixture theory, see Rajagopal and Tao (1995); Truesdell and Rajagopal (1999). Mixture models have been successfully used later on for the description of several biological systems and, in particular, for modelling biofilms (Clarelli et al., 2013; 2016; Zhang et al., 2008a, b).

In this article, we focus on the mathematical modelling of phototrophic biofilms of microalgae through mixture models with a special attention to the physiological involved mechanisms. We improve and adapt the previous mixture model for biofilms of cyanobacteria in a fountain, proposed by Clarelli et al. in Clarelli et al. (2013, 2016). Note that, from the analytical perspective, the existence of solutions for such mixture models has been established very recently and only for some simplified models (Bianchini and Natalini, 2016).

We consider three components in the mixture: microalgae, extra-cellular matrix and liquid. The liquid phase contains dissolved components, such as carbon dioxide, oxygen and substrate. In line with quota models (Mairet et al., 2011) usually used to describe growth limited by a nutrient, we consider separately the pool of carbon storage, mainly made of sugars and lipids, and the functional part of microalgae, composed of proteins, RNA, etc... The behaviour of each of the seven variables considered in the model is described by two conservation laws: mass balance equation, which accounts for mass transfers between the different components and gives the evolution of the component density, and force balance equation, which gives the evolution of momentum and contains physical properties of the phase. The model is supplemented by an incompressibility constraint, obtained from the total mass conservation. This constraint is expressed on the mean hydrodynamic velocity and leads to an hydrostatic pressure term in the force balance equations of the model. As in Clarelli et al. (2013); 2016), we keep the inertial terms in momentum equations to guarantee the hyperbolicity of the system and the finite speed of propagation of the front.

However, the adaptation of the model in Clarelli et al. (2013) to present context imposes several improvements : first, we consider a larger number of components and therefore we need to work with more velocities. Moreover, we take into account some components dissolved in the water, for which we add a diffusion term in the mass balance equations, leading to reaction-advection-diffusion equations. Finally, the main improvement is the fine description of the mass transfers between components, focusing on the biological mechanisms that drive the development of the biofilm, namely photosynthesis, respiration , functional biomass synthesis, extra-cellular matrix excretion and microalgae death. To do so, all these mechanisms are expressed under the form of macroscopic biochemical reactions and the kinetic of these reactions is carefully studied. To express the reaction rates, we need to identify clearly the influence of each of the components of the model. Some inhibiting factors or some threshold effects are described by kinetic laws, such as Monod's law (Monod, 1949) or Haldane's law (Andrews, 1968). In particular, we use Droop's model (Droop, 1968) in order to take into account an activation threshold and a saturation effect of an internal ratio for the photosynthesis reaction rate. Finally, combining all this information, we are able to define in an appropriate way the source terms of the mass balance equations. Note that this fine description brings us to consider an incompressibility constraint with a non zero right-hand side, unlike in Clarelli et al. (2013).

Once the model is established, we propose a numerical scheme in order to perform some accurate numerical simulations, using some finite differences techniques. This numerical scheme is presented in details in the appendices. The basis of the scheme relies on what has been done in Clarelli et al. (2013), that is to say we compute the hyperbolic part of the problem with a robust Riemann solver based on a relaxation scheme. The same difficulties as in Clarelli et al. (2013) have to be faced: first, in some regions, some phases may vanish. Unlike gas theory, where we can work in absence of vacuum, the situation when one phase or several phases vanish is relevant in a biological context. In such a case, the computation of the velocities has to be done carefully, using an implicit discretisation in time for the momentum equations. Another common difficulty between the two works is the computation of the pressure, linked to the treatment of the incompressibility constraint. As in Clarelli et al. (2013), we use a fractional step approach, based on Chorin-Temam projection method (Chorin, 1968; Temam, 1968), adapted to the particular incompressibility constraint we deal with. However, another difficulty arises in our case: the source terms appearing in the mass balance equations, built from the kinetic laws, may be stiff and lead to numerical instabilities. We therefore use a partially implicit time discretisation for some of the components in the source terms, which ensures that all the densities remain positive.

This numerical scheme enables us to present some numerical simulations in the one-dimensional case in order to study the influence of various parameters of the model, such as the value of the substrate supply or the parameters involved in the light modelling. More precisely, some tests are presented at the end of the article to show the effect of the intensity on the upper surface of the water, the absorption coefficient of light by the biofilm and the day-night variation of light. Some numerical simulations in the two-dimensional case have also been performed, but will be presented in a forthcoming article with the aim of comparing them with experimental results.

The paper is organised as follows: in the first section, we present the components considered in the mathematical model and we detail the physiological mechanisms, expressing them un-

der the form of macroscopic biochemical reactions. In the second section, we describe the equations that compose the model, namely the mass balance equations and the force balance equations. A subsection is devoted to the expression of the source terms for the mass balance equations, based on the previously mentioned chemical reactions. To do so, we need to define precisely in a third subsection the form of the reaction rates, taking into account all the factors that may enhance or inhibit the reactions. Finally, at the end of this section, we give estimates of the model parameters. We display, in the last section, some numerical results in the one-dimensional case, investigating the influence of several parameters on the model. Finally, conclusion and perspectives are given. Three appendices are dedicated respectively to the description of the numerical scheme, to supplementary numerical simulations and to further parameter estimation.

2. Description of the biological system

The model is designed to describe accurately the lipid production by microalgae within biofilms. We include the biochemical reactions that drive the growth of the biofilm and the production of extra-cellular matrix (ECM). This section is dedicated first to the presentation of the components that are described in our model.

2.1. Definition of the biofilm components

In a biofilm, micro algae are embedded within a self produced extra -cellular matrix. Microalgae and extra-cellular matrix are both organic compounds but they have some very different roles in the biofilm formation: photosynthesis takes place in the microalgae, whereas extra-cellular matrix is an inert component. Indeed, extra -cellular matrix is made of dead cells and extra-polymeric substance released by microalgae such as polysaccharides, proteins or DNA, see Xiao and Zheng (2016).

Photosynthesis supports inorganic carbon fixation, and thus growth of microalgae; it takes place in the chloroplasts. In line with other models (Bernard et al., 2013a; Mairet et al., 2011), we split the biomass into a functional biomass and the pool of carbon storage. On the one hand, the functional biomass gathers biosynthetic molecules such as proteins, nucleic acids and structural material. On the other hand, the pool of carbon storage is defined as the microalgae without the functional part and is mainly made of sugar, lipids and carbohydrates.

Consequently, the mathematical model under consideration contains four main constituents, that is to say: pool of carbon storage denoted by **A**, functional biomass denoted by **N**, extra-cellular matrix denoted by **E** and liquid phase denoted by **L**. Note that the two elements **A** and **N** form microalgae, that may be denoted by **M** when necessary. We also consider three main components dissolved in liquid phase which play an active role in biofilm growth and extra-cellular matrix production: carbon dioxide denoted by **C** (made by CO_2 and bicarbonate), oxygen denoted by **O** and substrate (here we consider inorganic nitrogen such as nitrate) denoted by **S**.

Before going further, let us detail the definition of **A, N** and **E**. Microalgae are mostly made of water: we consider that 90% of their mass is water. So components **A** and **N** represent the pool of carbon storage and the functional biomass within the associated liquid present inside the cellular membrane of microalgae. For example, the pool of carbon storage gathers sugars, lipids and carbohydrates with a part of the internal water of microalgae. It is assumed that water inside microalgae is proportionally divided into **A** and **N** according to their mass. Similarly the extra-cellular matrix is a tangle of polymers soaked in water so **E** denotes the ECM with internal water. Observe that liquid phase **L** represents the water outside of the biofilm and should not be confused with water trapped into biofilm.

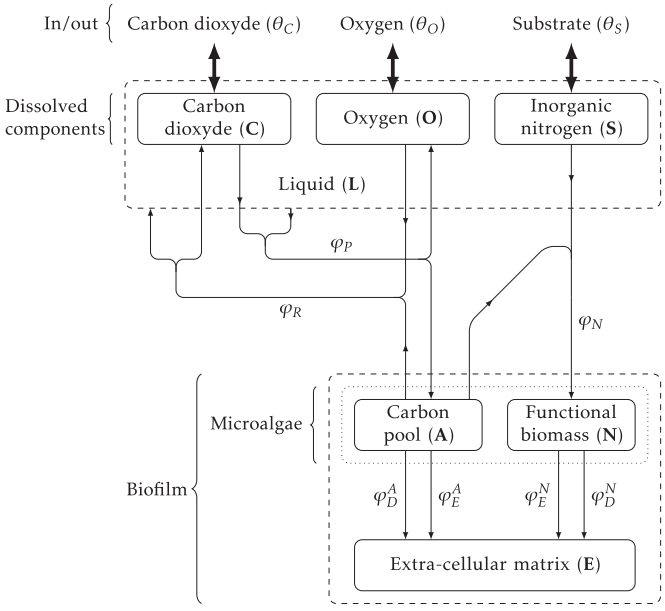

Fig. 1. Schematic representation of the model including the external supplies and the metabolic pathways.

Finally, let us notice that the effect of the light intensity is of course of great importance in order to model photosynthesis; in the following, light intensity is denoted by I.

2.2. Considered biological mechanisms

Now, let us describe the main mechanisms occurring during the formation of microalgae biofilms. Most of these mechanisms are well-known and well-understood for microalgae in planktonic phases, we make the hypothesis here that the same effects, for example of nutrients, are present for microalgae in a biofilm context. Note that a summary of these mechanisms is presented in Fig. 1.

2.2.1. Microalgae growth

The leading mechanism responsible for the biofilm development is photosynthesis, that is to say the absorption of the carbon dioxide dissolved in water using the light. More precisely, during the photosynthesis process, microalgae consume carbon dioxide and water, release oxygen and produce carbohydrates in order to fuel the metabolism. Inorganic carbon uptake depends on many factors and we summarise in what follows the overriding phenomena that occur during photosynthesis. First, the photosynthesis rate increases with the amount of reactants (carbon dioxide and water). Several studies highlight that this rate saturates when the carbon dioxide concentration exceeds a certain value. Then, the photosynthesis rate also increases with light intensity up to a threshold, above which it decreases due to photo-inhibition (Bernard, 2011; Eilers and Peeters, 1993); since biofilm develops during several days, it also benefits from a periodical enlightenment, following the day and night cycle. Another inhibiting factor for photosynthesis is the oxygen concentration (Costache et al., 2013) which can reach high concentrations in the very photosynthetically intensive processes. Finally, as explained previously, photosynthesis happens within the functional biomass and, therefore, the quota of functional biomass in the microalgae will affect the photosynthesis rate.

Moreover, when the microalgae are not illuminated, they use another source of energy provided by the respiration. The cells use

the oxygen dissolved in water to oxidise the carbohydrates contained in the pool of carbon storage of microalgae. During this process, carbon dioxide and water are released.

Finally, since we quantify the production of functional biomass, we consider that this process consumes the carbohydrates contained inside microalgae and the nitrate dissolved in the water.

2.2.2. Extra cellular matrix formation

Let us describe the different mechanisms that lead to the formation of extra-cellular matrix, which is composed both of dead cells and exopolysaccharides (EPS) released by microalgae.

First, part of the extra-cellular matrix is composed of EPS excreted by the microalgae. During the photosynthesis process, when microalgae are illuminated in the presence of carbon dioxide, they store carbon under the form of carbohydrates. Then, if nitrogen is available, they produce functional biomass and divide. However, in case of nitrogen starvation and imbalance between nitrogen and carbon fluxes, microalgae start to release polysaccharides (Staats et al., 2000), but also some parts of the functional biomass, composed of proteins.

The other mechanism which produces extra -cellular matrix is the death of microalgae. We assume that microalgae death rate depends on the dissolved oxygen concentration. When the oxygen concentration becomes smaller than a threshold, cell mortality is enhanced. On the opposite, the dissolved oxygen concentration released by photosynthesis can exceed three times the oxygen saturation in liquid at equilibrium. Together with photons, oxygen forms free radicals which are toxic for cells and induce mortality (Costache et al., 2013; Peng et al., 2013). When the microalgae die, the functional biomass and the pool of carbon storage contained in the cells are released and we assume that they entangled within the surrounding extra-cellular matrix.

2.3. Representations of the biological mechanisms under the form of macroscopic bioreactions

The aim of this subsection is to give a schematic representation of the five mechanisms considered in Sections 2.2.1 and 2.2.2. Fig. 1 presents an overview of the main mass fluxes considered in the model. These biochemical reactions involve a stoichiometry and reaction rates.

Macroscopic reactions are often not totally balanced, and their stoichiometry is rather given by pseudo-stoichio-metric coefficients taking into account losses that may occur during the reactions (Bernard and Bastin, 2005). In the following, pseudo-stoichiometric coefficients are denoted by η_P^ϕ (resp. η_R^ϕ, η_N^ϕ, η_E^ϕ and η_D^ϕ) for Photosynthesis (resp. Respiration, functional biomass synthesis, EPS excretion and microalgae Death) where ϕ stands for one of the components $\phi \in \{A, N, E, L, S, C, O\}$. Note that the values of all these parameters are fixed later on in Table 1.

Moreover, the reaction rate describes the number of units of the main synthesised product by unit of time. This function depends on several parameters, in particular the concentrations of reactants. In the following, we denote by φ_P (resp. φ_R, φ_N, φ_E, φ_D) the reaction rate for photosynthesis (resp. respiration, functional biomass synthesis, EPS excretion and microalgae death) and, in the following subsections, we will make precise for each reaction with which component we normalise the reaction rate. All these reaction rates will be modeled in details as source terms of the mass balance equations later on, in Section 3.2.2.

2.3.1. Photosynthesis

As described in Section 2.2.1, during photosynthesis, microalgae assimilate the carbon dioxide contained in liquid phase thanks to light. More precisely in the presence of light, microalgae consume carbon dioxide and liquid to produce sugar and reject oxygen. In terms of the components of Section 2.1, photosynthesis consumes **C** and **L** to produce **A** and **O**. Therefore, the schematic representation of photosynthesis is

$$\eta_P^C \mathbf{C} + \eta_P^L \mathbf{L} \xrightarrow{\varphi_P} \mathbf{A} + \eta_P^O \mathbf{O}, \tag{1}$$

where φ_P is the rate of carbon storage **A** production and η_P^ϕ for $\phi = C, L, O$ are the pseudo-stoichiometric coefficients of photosynthesis.

2.3.2. Respiration

In absence of light, respiration provides energy to the microalgae cells by consuming carbohydrates in the pool of carbon storage. The respiration process consumes carbohydrates contained into microalgae and oxygen dissolved in liquid to produce energy; this mechanism releases carbon dioxide and water. It can therefore be written under the following form:

$$\mathbf{A} + \eta_R^O \mathbf{O} \xrightarrow{\varphi_R} \eta_R^C \mathbf{C} + \eta_R^L \mathbf{L}, \tag{2}$$

where φ_R is the consumption rate of **A** and η_R^ϕ for $\phi = C, L, O$ are the pseudo-stoichiometric coefficients of respiration.

2.3.3. Functional biomass synthesis

Functional biomass is composed of nitrogen embedded into long carbon chains (proteins, DNA, RNA, ...). Carbon chains are provided by the pool of carbon storage **A**, whereas nitrogen comes from the substrate **S**.

The macroscopic reaction describing the synthesis of structural biomass (proteins, DNA, RNA,...) from both inorganic nitrogen and the product of photosynthesis **A** is summarised by the following macroscopic reaction:

$$\eta_N^A \mathbf{A} + \eta_N^S \mathbf{S} \xrightarrow{\varphi_N} \mathbf{N}, \tag{3}$$

where φ_N is rate of functional biomass **N** biosynthesis and η_N^A and η_N^S are the pseudo-stoichiometric coefficients for **A** and **S** of the synthesis of functional biomass.

2.3.4. Extra-polymeric substance (EPS) excretion

As explained in Section 2.1, extra-cellular matrix **E** constitutes a fundamental component of the biofilm and is mainly made of polysaccharides, proteins and nucleic acids, see Xiao and Zheng (2016). We assume that the polysaccharides released by microalgae come from the pool of carbon storage **A**, whereas proteins are derived from functional biomass **N**. Therefore EPS (extra-polymeric substrate) excretion is divided into two bioreactions:

$$\mathbf{A} \xrightarrow{\varphi_E^A} \mathbf{E}, \tag{4a}$$

$$\mathbf{N} \xrightarrow{\varphi_E^N} \mathbf{E}, \tag{4b}$$

where φ_E^A (resp. φ_E^N) is the reaction rate for the excretion of polysaccharides (resp. of functional biomass).

2.3.5. Microalgae death

Dead microalgae enter into the extra-cellular matrix. Consequently, the mortality can be represented by two reactions, one for the pool of carbon storage and the other one for the functional biomass, namely:

$$\mathbf{A} \xrightarrow{\varphi_D^A} \mathbf{E}, \tag{5a}$$

$$\mathbf{N} \xrightarrow{\varphi_D^N} \mathbf{E}, \tag{5b}$$

where φ_D^A and φ_D^N are the two reaction rates.

Table 1
Estimated values of the pseudo stoichiometric coefficients and of the maximal reaction rates used in the system described in subsection 3.5.

Name	Value	Considered mechanisms	Considered component	Ref.
η_P^A	1 kg**A**/kg**A**	Photosynthesis	Pool of carbon storage **A**	Section C.1
η_P^O	0.106 kg**O**/kg**A**	Photosynthesis	Oxygen **O**	Section C.1
η_P^C	0.146 kg**C**/kg**A**	Photosynthesis	Carbon dioxyde **C**	Section C.1
η_P^L	0.960 kg**L**/kg**A**	Photosynthesis	Liquid **L**	Section C.1
η_R^A	1 kg**A**/kg**A**	Respiration	Pool of carbon storage **A**	Section C.1
η_R^O	0.106 kg**O**/kg**A**	Respiration	Oxygen **O**	Section C.1
η_R^C	0.146 kg**C**/kg**A**	Respiration	Carbon dioxyde **C**	Section C.1
η_R^L	0.960 kg**L**/kg**A**	Respiration	Liquid **L**	Section C.1
η_N^A	1.66 kg**A**/kg**L**	Synthesis of functional biomass **N**	Pool of carbon storage	(Baroukh et al., 2014)
η_N^S	0.045 kg**S**/kg**L**	Synthesis of functional biomass **N**	Substrate **S**	(Baroukh et al., 2014)
μ_P	2 d^{-1}	Maximal photosynthesis rate		(Bernard, 2011; Bernard et al., 2013a)
μ_R	0.2 d^{-1}	Maximal respiration rate		(Edmundson and Huesemann, 2015)
μ_N	10.64 d^{-1}	Maximal functional biomass synthesis rate		(Mairet et al., 2011)
μ_E^A	0.3 d^{-1}	Maximal EPS excretion rate from **A**		(Sohm et al., 2011)
μ_E^N	0.1 d^{-1}	Maximal EPS excretion rate from **N**		Section C.2
μ_D	0.2 d^{-1}	Maximal microalgae death rate		(Serra-Maia et al., 2016)

3. Description of the mathematical model

In this section, we introduce a mathematical model describing the formation and the growth of a biofilm of microalgae together with the biofilm composition. All the phenomena mentioned in previous section will be integrated into the model. To avoid the mathematical complexity associated with the introduction of a physical interface between the biofilm and the external medium, we use the mixture theory framework, following Clarelli et al. (2013). This model is composed of a mass balance equation for each component coupled with force balance equations in which the physical properties of each phase are described. Since the mass balance equations are written in terms of volume fractions, the model includes a volume constraint, which can be expressed equivalently as an incompressibility constraint, in the spirit of Navier-Stokes incompressibility constraint. Notice that, since we are dealing with bio-chemical reactions, the expressions of the source terms for the mass balance equations are complex nonlinear functions which will be detailed in Section 3.2.

3.1. Mass balance equations

As mentioned in Section 2.1, we split the components considered in this model in two parts: on the one hand, the ones that constitute biofilm and liquid, and on the other hand, the ones dissolved in liquid.

3.1.1. Notations and conventions

In the following, we denote by $t \geq 0$ the time variable and $x \in \Omega$ the position with Ω the spatial domain under consideration which may be a subset of $\mathbb{R}$, $\mathbb{R}^2$ or $\mathbb{R}^3$.

Note that, although this article focuses on the one-dimensional case, our aim is to perform numerical simulations and comparisons with experiments in a 2D or 3D setting. Therefore, we present the following mathematical model in a general context.

For a component, we denote by ϕ its volume fraction, by ρ_ϕ the volumetric mass density, by v_ϕ its velocity and by Γ_ϕ the source term of the mass balance equation describing the evolution of its volume fraction. In particular, we denote by A (resp. N, E, L) the volume fraction of pool of carbon storage **A** (resp. of functional biomass **N**, extra-cellular matrix **E** and liquid **L**), namely the volume occupied by the component in an elementary volume $\mathbb{V}$ divided by the volume of $\mathbb{V}$.

Remark that pool of carbon storage **A** and functional biomass **N** are both parts of microalgae; therefore, we use for these two elements the same density, denoted by ρ_M and the same velocity called v_M, where **M** stands for the whole microalgae.

3.1.2. Mass balance equations for biofilm and liquid

Following Clarelli et al. (2013), the evolution with respect to time of the mass of one of the components verifies

$$\partial_t\left(\rho_\phi \phi\right) + \nabla_X \cdot \left(\rho_\phi \phi v_\phi\right) = \Gamma_\phi.$$

Assuming that this component is incompressible, that is to say that ρ_ϕ is constant in time and space, we deduce for $\phi = A, N, E$ and L, the corresponding mass balance equations:

$$\partial_t A + \nabla_X \cdot (A v_M) = \Gamma_A/\rho_M, \tag{6a}$$

$$\partial_t N + \nabla_X \cdot (N v_M) = \Gamma_N/\rho_M, \tag{6b}$$

$$\partial_t E + \nabla_X \cdot (E v_E) = \Gamma_E/\rho_E, \tag{6c}$$

$$\partial_t L + \nabla_X \cdot (L v_L) = \Gamma_L/\rho_L. \tag{6d}$$

3.1.3. Incompressibility constraint

Assuming that the volume of the dissolved components is negligible, for any time $t \geq 0$ and position $X \in \Omega$, the volume fractions A, N, E and L satisfy the volume condition:

$$A(t,X) + N(t,X) + E(t,X) + L(t,X) = 1. \tag{7}$$

Consequently, by summing the four Eqs. (6) and using condition (7), we obtain an incompressibility constraint:

$$\nabla_X \cdot ((A+N)v_M + E v_E + L v_L) = \frac{\Gamma_A + \Gamma_N}{\rho_M} + \frac{\Gamma_E}{\rho_E} + \frac{\Gamma_L}{\rho_L}. \tag{8}$$

Let us notice that we can work with the two Eqs. (7) and (8) in the following, omitting therefore the mass balance equation for liquid (6d).

3.1.4. Mass balance equations for components dissolved in liquid

Let us now consider the components dissolved in liquid phase, that is to say substrate **S**, carbon dioxide **C** and oxygen **O**. Since their volume fraction is negligible, we consider their mass fraction, denoted by S, C and O, that is to say the mass contained in liquid divided by the mass of liquid. Their volumetric mass density is the same as the liquid density ρ_L and their velocity is driven by the velocity of liquid phase v_L. Moreover, in addition to the convection phenomenon, we take into account the diffusion and we add a diffusive term in the mass balance equations. Following Ambrosi and Preziosi (2002) we assume that the diffusion follows the Fick's law, namely the diffusive flux is assumed to be proportional to the concentration gradient of dissolved component in liquid. Therefore the

local formulation of the mass balance equation for the components dissolved in liquid phase writes as

$$\partial_t(SL) + \nabla_X \cdot (SL v_L) - \nabla_X \cdot (\delta_S L \nabla_X S) = \Gamma_S/\rho_L, \tag{9a}$$

$$\partial_t(CL) + \nabla_X \cdot (CL v_L) - \nabla_X \cdot (\delta_C L \nabla_X C) = \Gamma_C/\rho_L, \tag{9b}$$

$$\partial_t(OL) + \nabla_X \cdot (OL v_L) - \nabla_X \cdot (\delta_O L \nabla_X O) = \Gamma_O/\rho_L, \tag{9c}$$

where δ_ϕ for $\phi = S, C, O$ are the diffusion coefficients.

3.2. Source terms and reaction rates

In this section, we will make precise the form of the source terms that appear on the right-hand side of equations (6) and (9) and that describe the mechanisms presented in Section 2.3. We will detail this expression for each component in the following subsection and then we will give the expressions of the reaction rates that may depend on several factors.

Remark that some simplifications are made to derive the source terms of the mass equations, since no detachment process is taken into account. We make therefore the assumption that no detachment occurs since no evidence on how a biofilm get detached is known for the moment.

3.2.1. Source terms

Pool of carbon storage **A** is a product of photosynthesis, see Section 2.3.1, with reaction rate φ_P. Moreover, according to Section 2.3.2, 2.3.3, 2.3.4 and 2.3.5, it is a reactant for all the other mechanisms: **A** is consumed by respiration with rate φ_R (see reaction (2)), by synthesis of functional biomass (3) with rate $\eta_N^A\varphi_N$, by the EPS excretion (4a) with rate φ_E^A and by microalgae death (5a) with rate φ_D^A. By combining all these terms, we obtain that the source term for **A** can be written as:

$$\Gamma_A = \varphi_P - \varphi_R - \eta_N^A\varphi_N - \varphi_E^A - \varphi_D^A. \tag{10a}$$

Now, considering Section 2.3.3, functional biomass **N** is produced with rate φ_N. However, the loss of functional biomass is due to EPS (extra-polymeric substance) excretion with rate φ_E^N and to mortality with rate φ_D^N, see reactions (4b) and (5b). Therefore, we can define the source term for **N** as:

$$\Gamma_N = \varphi_N - \varphi_E^N - \varphi_D^N. \tag{10b}$$

Extra-cellular matrix **E** is only produced and comes from two mechanisms: EPS excretion and mortality. Both can use either the pool of carbon storage or the functional biomass as a reactant. In all cases, according to reations (4a), (4b), (5a) and (5b), pseudo stoichiometric coefficients are equal to 1 and we obtain the following source term:

$$\Gamma_E = \varphi_E^A + \varphi_E^N + \varphi_D^A + \varphi_D^N. \tag{10c}$$

Water which is the main component of liquid phase **L** is a reactant in photosynthesis with rate $\eta_P^L\varphi_P$ and a product in respiration with rate $\eta_R^L\varphi_R$, see reactions (1) and (2), so:

$$\Gamma_L = \eta_R^L\varphi_R - \eta_P^L\varphi_P. \tag{10d}$$

Now, substrate **S** is only consumed by functional biomass synthesis (3), with rate $\eta_N^S\varphi_N$; thus, we define the source term for **S** as:

$$\Gamma_S = -\eta_N^S\varphi_N. \tag{10e}$$

Carbon dioxide **C**, as liquid, is a reactant for photosynthesis (1) and a product of the respiration process (2); therefore we set:

$$\Gamma_C = \eta_R^C\varphi_R - \eta_P^C\varphi_P. \tag{10f}$$

Finally, oxygen **O** is released by the photosynthesis mechanism (1) with rate $\eta_P^O\varphi_P$ and consumed by the respiration mechanism with rate $\eta_R^O\varphi_R$. Therefore, the source term for **C** can be written as:

$$\Gamma_O = \eta_P^O\varphi_P - \eta_R^O\varphi_R. \tag{10g}$$

3.2.2. Expressions of reaction rates

Now, in this section, let us present the expressions of the reaction rates introduced in Section 2.3 to quantify mass exchanges between model components.

These laws combine dimensionless elementary functions with values in the interval [0, 1]. Each reaction rate is therefore a product of elementary functions multiplied by the maximal rate per unit of time. In what follows, this maximal rate is called μ_α where α represents the considered mechanism; the estimated values of these rates are given in Table 1.

Note that some mechanisms may depend on the intra-cellular quota Q defined by

$$Q = N/(N + A),$$

which represents the amount of functional biomass per unit of micro algae biomass. In particular, this quota will be used to express the photosynthesis rate.

Photosynthesis rate. Photosynthesis (1) rate is the most complex mechanism since its reaction rate is driven by all components except substrate. It is also obviously influenced by the light intensity, denoted by I. For the reader's convenience, we consider separately the effects of each component and we denote by f_ϕ, with $\phi = Q, N, L, C, O, I$, the corresponding elementary function which depends only on ϕ and takes values in [0, 1], except f_N. The expression for the photosynthesis rate will finally be the product

$$\varphi_P = \mu_P f_N f_Q f_L f_C f_O f_I, \tag{11}$$

where μ_P is the maximal photosynthesis rate per unit of microalgae and unit of time.

First, we assume that production rate of carbon storage is linearly dependent on the functional biomass (Lemesle and Mailleret, 2008), so f_N is equal to $\rho_M N$ up to a constant k, to be determined. The maximal photosynthesis rate μ_P corresponds to the maximal value for

$$\varphi_P/(\rho_M(N + A)),$$

which is also equal to

$$\mu_P k(N/(N + A))_{max} = \mu_P k Q_{max}$$

according to Eq. (11). Therefore $k = 1/Q_{\max}$ and we set

$$f_N = \rho_M N/Q_{max} \tag{12a}$$

with $Q_{\max}$ a threshold above which the functional biomass production is stopped, that is to say the quota Q does not have any impact on the photosynthesis rate if $Q \geq Q_{\max}$.

Moreover, as mentioned in Section 2.2.1, photosynthesis is performed by chloroplasts, contained in the functional biomass. Their quantity increases with the intra-cellular quota and photosynthesis occurs when Q exceeds a given threshold $Q_{\min}$, which can be described by Droop model (Bernard and Gouzé, 1995; Droop, 1968). We obtain therefore:

$$f_Q = \frac{Q_{max}}{Q_{max} - Q_{min}} \max\left\{0, 1 - \frac{Q_{min}}{\min\{Q, Q_{max}\}}\right\}, \tag{12b}$$

which implies that $f_Q = 0$ for $Q < Q_{\min}$ and $f_Q = 1$ when $Q > Q_{\max}$.

Now, to take into account the impact of carbon dioxide and liquid, we use a Michaëlis-Menten law which reflects an almost

linear increase for a low amount of reactants and a threshold effect when reactants are in excess. The photosynthesis rate depends consequently on

$$f_C = \frac{C}{\mathcal{K}_C + C}, \qquad f_L = (\mathcal{K}_L + 1)\frac{(\mathcal{K}_L + 1)L}{\mathcal{K}_L + L} \tag{12c}$$

with $\mathcal{K}_C$ and $\mathcal{K}_L$ the half saturation constants of carbon dioxide and liquid. The coefficient $\mathcal{K}_L + 1$ ensures that $\max\{f_L(L), L \in [0,1]\} = 1$.

Moreover, according to Costache et al. (2013), photosynthesis is inhibited when the oxygen concentration is too high and interferes with Calvin cycle (photorespiration). We model this effect with the following sigmoid function:

$$f_O = \frac{1}{1 + \left(\frac{O}{\mathcal{K}_O}\right)^{\alpha}} \tag{12d}$$

with $\mathcal{K}_O$ the half saturation constant and $\alpha > 0$ a strictly positive parameter that determines the stiffness of the sigmoid.

Finally, we need to consider the impact of light intensity. We assume here that the change of temperature does not have a major impact on the biofilm development, for simplicity reasons. However, this assumption is unreasonable and would need to be studied in a future work. In line with many models, we use Haldane's law (Eilers and Peeters, 1993; Thébault and Rabouille, 2003), that is to say:

$$f_I = 2(1 + \mathcal{K}_I)\frac{\hat{I}}{\hat{I}^2 + 2\mathcal{K}_I\hat{I} + 1}, \qquad \text{where } \hat{I} = \frac{I}{I_{opt}}, \tag{12e}$$

with I the light intensity, I_{opt} the optimal light intensity and $\mathcal{K}_I$ a parameter.

The received light intensity I is a space-dependent parameter, since light is absorbed according to the various layers it encounters. So local light intensity $I(t, x, y, z)$ depends on the incident light intensity on the upper surface of water $I_0(t, x, y)$ and on an attenuation coefficient, which evolves with the depth and the composition of the above medium. Precisely, the attenuation coefficient at position $X = (x, y, z)$ depends on the depth and on the medium composition at points (x, y, ξ) for $z \le \xi \le H$, with H the height of the domain.

Following Stomp et al. (0000), we can describe the received light intensity by:

$$I(t,X) = I_0(t,x,y)\exp\left(-\int_z^H \tau_L L(t,x,y,\xi) + \tau_M(A(t,x,y,\xi) + N(t,x,y,\xi) + E(t,x,y,\xi))d\xi\right), \tag{13}$$

where τ_L and τ_M are the absorption coefficients of liquid and biofilm, estimated in Table 2.

Finally, by combining (12a) to (12e), we deduce the form of the photosynthesis rate, that is to say:

$$\varphi_P = \frac{\mu_P\rho_M}{Q_{max} - Q_{min}} N \frac{C}{\mathcal{K}_C + C}\frac{(\mathcal{K}_L + 1)L}{\mathcal{K}_L + L}\frac{1}{1 + \left(\frac{O}{\mathcal{K}_O}\right)^{\alpha}} \max\left\{0, 1 - \frac{Q_{min}}{\min\{Q, Q_{max}\}}\right\}\frac{2(1 + \mathcal{K}_I)\hat{I}}{\hat{I}^2 + 2\mathcal{K}_I\hat{I} + 1}. \tag{14a}$$

Respiration rate. Respiration rate depends on the oxygen and the pool of carbon storage, see Section 2.3.2. We assume that φ_R depends linearly on the pool of carbon storage $\rho_M A$ and that the Michaëlis-Menten's law applies for the dependence on oxygen; we denote by $\mathcal{K}_R$ the half saturation constant for the oxygen and by μ_R the maximal respiration rate. Thus, we obtain the following form for the respiration rate:

$$\varphi_R = \mu_R\rho_M A\frac{O}{\mathcal{K}_R + O}. \tag{14b}$$

Functional biomass synthesis rate. The functional biomass is synthesised thanks to a pool of enzymes. Thus φ_N (see Section 2.3.3) is assumed to depend linearly on the quantity of functional biomass $\rho_M N$. It also depends on the availability of the inorganic nitrogen and of the pool of carbon storage. In line with Bougaran et al. (2010) we also assume that nitrogen uptake stops depending on the cell nitrogen quota. As for the Droop model, the influence of the substrate **S** can be modelled by Michaëlis-Menten's kinetic with the half saturation constant $\mathcal{K}_S$.

Inorganic nitrogen is uptaken up to a threshold where intracellular quota reaches a maximum value $Q \geqslant Q_{\max}$. Therefore, we set, as in Bougaran et al. (2010):

$$\varphi_N = \mu_N\rho_M N\frac{S}{\mathcal{K}_S + S}\max\left\{0, \frac{Q_{max} - \max\{Q, Q_{min}\}}{Q_{max} - Q_{min}}\right\}, \tag{14c}$$

with μ_N the maximal rate of functional biomass synthesis. Note that $\varphi_N = 1$ for Q smaller than $Q_{\min}$ and $\varphi_N = 0$ when Q is greater than $Q_{\max}$.

EPS excretion rates. The rate of EPS excreted from the pool of carbon storage (resp. from the pool of functional biomass) φ_E^A (resp. φ_E^N) is assumed to be proportional to the quantity of the pool of carbon storage (resp. functional biomass) contained in microalgae. Both mechanisms are the same but excretion is lower for the EPS coming from functional biomass. So, the maximal excretion rate μ_E^N for the EPS coming from **N** in the reaction (4b) is smaller than the maximal excretion rate μ_E^A for EPS coming from **A** in reaction (4a) – their values are estimated in Table 1. Moreover, we assume that the EPS excretion rate is due to an imbalance between nitrogen and carbon pathways, and that it is therefore enhanced by low nitrogen quota. Combining all these effects, we obtain:

$$\varphi_E^A = \mu_E^A\rho_M A\max\left\{0, \frac{Q_{max} - \max\{Q, Q_{min}\}}{Q_{max} - Q_{min}}\right\}, \tag{14d}$$

$$\varphi_E^N = \mu_E^N\rho_M N\max\left\{0, \frac{Q_{max} - \max\{Q, Q_{min}\}}{Q_{max} - Q_{min}}\right\}. \tag{14e}$$

Microalgae death rates. Finally, the microalgae death rates φ_D^A and φ_D^N introduced in Section 2.3.5 are two parts of the same mechanism. Therefore, they induce both a linear decrease of biomass. Thus φ_D^A is proportional to the quantity of the pool of carbon storage and φ_D^N to the quantity of functional biomass. The variations of the death rates are driven essentially by the dissolved oxygen concentration: if the oxygen concentration is below the reference concentration $\mathcal{K}_D$, the mortality of microalgae increases. On the opposite, at high oxygen concentration death rate is larger. Consequently the death rate depends on the ratio between the oxygen concentration and the optimal oxygen concentration: $\hat{O} = O/\mathcal{K}_D$. In order to model a quasi linear decrease of the death for $O < \mathcal{K}_D$ we use a modified Michaëlis-Menten's law:

$$f_D(\hat{O}) = 1 - \frac{\beta\hat{O}}{\hat{O}^{\beta} + \beta - 1} \tag{14f}$$

with $\beta > 1$ a parameter estimated in Table 2, that settles the stiffness of the increase of the death rate for $O > \mathcal{K}_D$. In order to define β, we assume that the death induced by oxygen excess is triggered for the same oxygen saturation as the photosynthesis inhibition. Observe that we put $1 - \beta$ in the denominator in order that f_D remains in [0, 1] for $\hat{O} \geqslant 0$ and $f_D(1) = 0$. Finally we set:

$$\varphi_D^A = \mu_D\rho_M A\left(1 - \frac{\beta\hat{O}}{\hat{O}^{\beta} + \beta - 1}\right), \tag{14g}$$

$$\varphi_D^N = \mu_D\rho_M N\left(1 - \frac{\beta\hat{O}}{\hat{O}^{\beta} + \beta - 1}\right), \tag{14h}$$

where μ_D is the maximal mortality rate.

Table 2
Estimated values of the biological and physical parameters used in the system described in subsection 3.5.

Name	Value	Interpretation	Ref.
$\mathcal{K}_O$	$3.2 \cdot 10^{-5}$ kg**O**/kg**L**	Oxygen half saturation constant in photosynthesis	(Costache et al., 2013)
α	14	Stiffness of the sigmoid for the oxygen in photosynthesis	(Costache et al., 2013)
$\mathcal{K}_L$	0.5	Liquid half saturation constant in photosynthesis	(Lange et al., 1994)
$\mathcal{K}_C$	$4.4 \cdot 10^{-6}$ kg**C**/kg**L**	Inorganic carbon half saturation constant in photosynthesis	(Novak and Brune, 1985)
$\mathcal{K}_I$	0.1	Light parameter	(Clarelli et al., 2013; Stomp et al., 0000)
I_{opt}	100 μmolm^{-2}s^{-1}	Optimal light intensity	(Clarelli et al., 2013; Stomp et al., 0000)
$\mathcal{K}_R$	$1 \cdot 10^{-6}$ kg**O**/kg**L**	Oxygen half saturation constant in respiration	(Henze et al., 1987)
$\mathcal{K}_S$	$6.2 \cdot 10^{-8}$ kg**L**/kg**L**	Substrate half saturation constant in functional biomass synthesis	(Bernard et al., 2013a)
$\mathcal{K}_D$	$7.2 \cdot 10^{-6}$ kg**O**/kg**L**	Oxygen half saturation constant for microalgae death	Section C.4
β	1.8352	Stiffness of the increase of the death rate in mortality	Section C.4
$Q_{\min}$	$5.82 \cdot 10^{-2}$	Minimal threshold of functional biomass quota	(Mairet et al., 2011)
$Q_{\max}$	$1.57 \cdot 10^{-1}$	Maximal threshold of functional biomass quota	(Mairet et al., 2011)
ρ_M	1.090 kg L^{-1}	Volumetric mass density of microalgae	(Gudin and Chaumont, 1991)
ρ_E	1.090 kg L^{-1}	Volumetric mass density of EPS	C.3
ρ_L	1.025 kg L^{-1}	Volumetric mass density of liquid	
θ_S	$2-5 \cdot 10^{-5}$ kg**S**/kg**L**	Substrate intake	(Bernard et al., 2013a; Mairet et al., 2011)
θ_C	$2-14 \cdot 10^{-5}$ kg**C**/kg**L**	Inorganic carbon intake	(Bernard et al., 2013a)
θ_O	$7.2 \cdot 10^{-6}$ kg**O**/kg**L**	Oxygen intake	(Rubio et al., 1999)
δ_S	$1.47 \cdot 10^{-4}$ m^{2}d^{-1}	Substrate diffusion coefficient	(Wolf et al., 2007)
δ_C	$1.80 \cdot 10^{-4}$ m^{2}d^{-1}	Inorganic carbon diffusion coefficient	(Zeebe, 2011)
δ_O	$1.98 \cdot 10^{-4}$ m^{2}d^{-1}	Oxygen diffusion coefficient	(Wolf et al., 2007)
τ_L	0.1 m^{-1}	Light absorption coefficient for **L**	(Clarelli et al., 2013; 2016; Stomp et al., 0000)
τ_M	$2.5 \cdot 10^4$ m^{-1}	Light absorption coefficient for **M**	(Clarelli et al., 2013; 2016; Zippel et al., 2007)
m_{ML}	20 kg m^{3}d^{-1}	Friction coefficient of **M** over **L**	(Clarelli et al., 2013; 2016)
m_{EL}	20 kg m^{3}d^{-1}	Friction coefficient of **E** over **L**	(Clarelli et al., 2013; 2016)
m_{ME}	20 kg m^{3}d^{-1}	Friction coefficient of **M** over **E**	(Clarelli et al., 2013; 2016)
γ_M	$1.5 \cdot 10^{-7}$ kg m^{-1}d^{-2}	Tensor coefficient for microalgae **M**	(Clarelli et al., 2013; 2016)
γ_E	$1.5 \cdot 10^{-7}$ kg m^{-1}d^{-2}	Tensor coefficient for extra-cellular matrix **E**	(Clarelli et al., 2013; 2016)

3.3. Force balance equations

In this section, we establish some equations to compute the velocities used in the mass balance equations. To do so, we write some evolution equations for the momentum thanks to some force balance considerations. Following what we have done in Section 3.1, we consider the three following velocities: velocity of microalgae v_M, velocity of extra-cellular matrix v_E and liquid velocity v_L. Keeping the notations of Section 3.1 and following Clarelli et al. (2013), for $\phi = M, E$ or L, the evolution in time and space of momentum satisfies

$$\begin{aligned}\partial_t\left(\rho_\phi \phi v_\phi\right) + \nabla_X \cdot \left(\rho_\phi \phi v_\phi \otimes v_\phi\right) = \\ -\phi \nabla_x P - \nabla_X \cdot \left(\gamma_\phi \phi\right) + m_\phi + \Gamma_\phi v_\phi,\end{aligned} \tag{15}$$

where P is the hydrostatic pressure, γ_ϕ the elastic tensor coefficient, m_ϕ is the excess interaction force and $\Gamma_\phi v_\phi$ source of momentum resulting from mass exchanges. The stress tensor is assumed here to be linear and is chosen to be as simple as possible, since we still do not know what is the visco-elastic structure of a microalgae biofilm.

Moreover, in a close mixture system, the sum of the momentum supply due to the interaction forces and of the momentum transfers caused by the mass exchanges is equal to zero. So, as in Clarelli et al. (2013), relation

$$m_L + \Gamma_L v_L = -(m_M + (\Gamma_A + \Gamma_N) v_M + m_E + \Gamma_E v_E) \tag{16}$$

holds. In addition, we make the classical assumption that the elastic tensor coefficient is present only in solid components Rajagopal and Tao (1995). Thus, in liquid phase, the only external force is the hydrostatic pressure in order to have liquid at rest in absence of biofilm. Consequently, using Eq. (16) to simplify Eq. (15) for $\phi = L$, we deduce that the force balance equation for liquid phase can be written as:

$$\begin{aligned}\partial_t(\rho_L L v_L) + \nabla_X \cdot (\rho_L L v_L \otimes v_L) = \\ -L \nabla_x P - m_M - m_E - \Gamma_M v_M - \Gamma_E v_E.\end{aligned} \tag{17}$$

Finally, following Clarelli et al. (2013), we assume that the contact forces are proportional to the relative difference between the velocities of the components according to Darcy's law, and are symmetric, for example $m_{EM} = m_{ME}$. The friction coefficients m_{ML}, m_{ME}, m_{EL} and m_{EM} are experimental parameters and are estimated in Table 2.

To sum up, from Eqs. (15) and (17), we deduce that force balance equations are equal to:

$$\begin{aligned}&\partial_t((A+N)v_M) + \nabla_X \cdot ((A+N) v_M \otimes v_M) = \\ &\frac{1}{\rho_M}\Big(-(A+N)\nabla_x P - \nabla_X \cdot \left(\gamma_M (A+N)\right) \\ &- m_{ML}(v_M - v_L) - m_{ME}(v_M - v_E) + \Gamma_M v_M\Big),\end{aligned} \tag{18a}$$

$$\begin{aligned}&\partial_t(E v_E) + \nabla_X \cdot (E v_E \otimes v_E) = \frac{1}{\rho_E}(-E\nabla_x P \\ &- \nabla_X \cdot (\gamma_E E) - m_{EL}(v_E - v_L) + m_{ME}(v_M - v_E) \\ &+ \Gamma_E v_E),\end{aligned} \tag{18b}$$

$$\begin{aligned}&\partial_t(L v_L) + \nabla_X \cdot (L v_L \otimes v_L) = \frac{1}{\rho_L}(-L\nabla_x P \\ &+ m_{ML}(v_M - v_L) + m_{EL}(v_E - v_L) - \Gamma_M v_M \\ &- \Gamma_E v_E).\end{aligned} \tag{18c}$$

3.4. Boundary conditions

We complement this system with some boundary conditions as follows: we impose Neumann boundary conditions for the components constituting biofilm and for the liquid. For components dissolved in liquid phase, we also impose Neumann boundary conditions on all boundaries except on the boundary on top, where we impose some non homogeneous Dirichlet boundary conditions. These boundary conditions stand for external supply of substrate coming from the top of the domain.

The definition of the boundary conditions for the velocities requires more attention. Indeed by integrating the incompressibility constraint (8) on the whole domain Ω and using Stokes' theorem, we get the following compatibility condition

$$\int_{\partial\Omega} ((A+N)v_M + Ev_E + Lv_L)\cdot\vec{n}\, d\nu = \int_{\Omega}\left(\frac{\Gamma_A+\Gamma_N}{\rho_M}+\frac{\Gamma_E}{\rho_E}+\frac{\Gamma_L}{\rho_L}\right) d\omega.$$

In order to satisfy this compatibility condition, we impose for all the velocities some no flux boundary conditions on each boundary except on the top of the domain where the flux is imposed so that the compatibility condition holds.

3.5. Complete system of PDEs in 1D

In this subsection, let us summarise the full set of equations we derived in previous subsections. On the one dimensional domain $\Omega = [0, L_x]$ the full system consists in mass balance equations (6) – (9) coupled with source terms (10) and reaction rates (14), force balance equations (18), condition (7) and the incompressibility constraint (8), complemented by boundary conditions:

Reaction rates

$$\varphi_P = \frac{\mu_P\rho_M}{Q_{max}-Q_{min}}\frac{C}{\mathcal{K}_C+C}\frac{(\mathcal{K}_L+1)L}{\mathcal{K}_L+L}\frac{1}{1+\left(\frac{O}{\mathcal{K}_O}\right)^{\alpha}} N\max\left\{0, 1-\frac{Q_{min}}{\min\{Q,Q_{max}\}}\right\}\frac{2(1+\mathcal{K}_I)\hat{I}}{\hat{I}^2+2\mathcal{K}_I\hat{I}+1},$$

$$\varphi_R = \mu_R\rho_M A\frac{O}{\mathcal{K}_R+O},$$

$$\varphi_N = \mu_N\rho_M N\frac{S}{\mathcal{K}_S+S}\max\left\{0, \frac{Q_{max}-\max\{Q,Q_{min}\}}{Q_{max}-Q_{min}}\right\},$$

$$\varphi_E^A = \mu_E^A\rho_M A\max\left\{0, \frac{Q_{max}-\max\{Q,Q_{min}\}}{Q_{max}-Q_{min}}\right\},$$

$$\varphi_E^N = \mu_E^N\rho_M N\max\left\{0, \frac{Q_{max}-\max\{Q,Q_{min}\}}{Q_{max}-Q_{min}}\right\},$$

$$\varphi_D^A = \mu_D\rho_M A\left(1-\frac{\beta\hat{O}}{\hat{O}^{\beta}+\beta-1}\right),$$

$$\varphi_D^N = \mu_D\rho_M N\left(1-\frac{\beta\hat{O}}{\hat{O}^{\beta}+\beta-1}\right),$$

$$Q = N/(N+A),\quad \hat{O} = O/\mathcal{K}_D,\quad \hat{I} = I/I_{opt},$$

$$I(t,x) = I_0(t)\exp\left(-\int_z^H \tau_L L(t,\xi) + \tau_M(A(t,\xi)+N(t,\xi)+E(t,\xi))d\xi\right),$$

Source terms

$$\Gamma_A = \varphi_P-\varphi_R-\eta_N^A\varphi_N-\varphi_E^A-\varphi_D^A,$$

$$\Gamma_N = \varphi_N-\varphi_E^N-\varphi_D^N,\ \Gamma_E = \varphi_E^A+\varphi_E^N+\varphi_D^A+\varphi_D^N,$$

$$\Gamma_L = \eta_R^L\varphi_R-\eta_P^L\varphi_P,\quad \Gamma_C = \eta_R^C\varphi_R-\eta_P^C\varphi_P,$$

$$\Gamma_S = -\eta_N^S\varphi_N,\quad \Gamma_O = \eta_P^O\varphi_P-\eta_R^O\varphi_R,$$

Mass balance equations

$$\partial_t A+\partial_x(Av_M) = \Gamma_A/\rho_M,$$

$$\partial_t N+\partial_x(Nv_M) = \Gamma_N/\rho_M,$$

$$\partial_t E+\partial_x(Ev_E) = \Gamma_E/\rho_E,$$

Volume constraint and incompressibility constraint

$$A+N+E+L = 1,$$

$$\partial_x((A+N)v_M+Ev_E+Lv_L) = \frac{\Gamma_A+\Gamma_N}{\rho_M}+\frac{\Gamma_E}{\rho_E}+\frac{\Gamma_L}{\rho_L},$$

Mass balance equations for dissolved components

$$\partial_t(SL)+\partial_x(SLv_L)-\partial_x(\delta_S L\partial_x S) = \frac{\Gamma_S}{\rho_L},$$

$$\partial_t(CL)+\partial_x(CLv_L)-\partial_x(\delta_C L\partial_x C) = \frac{\Gamma_C}{\rho_L},$$

$$\partial_t(OL)+\partial_x(OLv_L)-\partial_x(\delta_O L\partial_x O) = \frac{\Gamma_O}{\rho_L},$$

Force balance equations

$$\partial_t((A+N)v_M)+\partial_x\left((A+N){v_M}^2\right) = \frac{1}{\rho_M}\Big(-(A+N)\partial_x P-\partial_x\left(\gamma_M(A+N)\right) - m_{ML}(v_M-v_L)-m_{ME}(v_M-v_E) + (\Gamma_A+\Gamma_N)v_M\Big),$$

$$\partial_t(Ev_E)+\partial_x\left(E{v_E}^2\right) = \frac{1}{\rho_E}\left(-E\partial_x P-\partial_x(\gamma_E E) - m_{EL}(v_E-v_L)+m_{ME}(v_M-v_E)+\Gamma_E v_E\right),$$

$$\partial_t(Lv_L)+\partial_x\left(L{v_L}^2\right) = \frac{1}{\rho_L}\Big(-L\partial_x P + m_{ML}(v_M-v_L)+m_{EL}(v_E-v_L) - (\Gamma_A+\Gamma_N)v_M-\Gamma_E v_E\Big),$$

Boundary conditions

$$\partial_x\phi(t,0) = 0,\quad \partial_x\phi(t,L_x) = 0,\quad \phi = A,N,E,L,$$

$$v_\phi(t,0) = 0,\quad \phi = M,E,L,$$

$$v_\phi(t,L_x) = \int_0^{L_x}\left(\frac{\Gamma_A+\Gamma_N}{\rho_M}+\frac{\Gamma_E}{\rho_E}+\frac{\Gamma_L}{\rho_L}\right)dx,\quad \phi = M,E,L,$$

$$\partial_x(\phi L)(t,0) = 0,\quad \partial_x(\phi L)(t,L_x) = \theta_\phi,\quad \phi = S,C,O,$$

where θ_S, θ_C, θ_O are the external supplies of substrate, carbon and oxygen.

3.6. Parameters estimation

The parameter values chosen for the simulations are presented in Table 1 and 2. Most of the parameters are derived from the literature and some parameters are derived from the state of the art on photosynthesis. The half saturation constants used in the reaction rates are generally expressed in terms of concentration in kg L^{-1} or in mol L^{-1}. However, in our case, the amount of each component is dimension free and the values given in Table 2 are therefore converted, using the volumetric mass density or the molar mass.

For the photosynthesis and the respiration processes, the pseudo-stoichiometric coefficients are estimated using the molar mass of the components involved in the reactions and considering that, during the reaction, around 90% of the exchanged matter is water.

Moreover, the values of $\mathcal{K}_O$ and α are chosen to fit the curve proposed in Costache et al. (2013) as a sigmoid function. Finally, the values of Q_{min} and Q_{max} are deduced from Mairet et al. (2011), where the range of N/A is estimated. Details on parameters estimation are given at Appendix C.

3.7. Homogeneous steady states

In this subsection, we consider solutions which are constant in time and space. They satisfy $\Gamma_\phi = 0$ for $\phi = A, N, E, L, S, C, O$. Since functions φ_E^A, φ_E^N, φ_D^A and φ_D^N are positive, see Sec. 3.5, $\Gamma_E = 0$ leads to $\varphi_D^A = \varphi_D^N = 0$ and to $A = N = 0$, using Eq. (14g) and (14h). Consequently, the only homogeneous steady states of the system are steady states without microalgae, which is not of interest for our study.

4. Numerical simulations

In this section, we present some numerical results in the one dimensional case. Although biofilms are complex 3D structures, it is very useful to make preliminary 1D tests to check the efficiency of the model and to analyse solutions of the system. For example, in our case, the following simulations help to understand effects of the limiting processes present in the expression of the reaction rates and the role of some key parameters. More precisely, after giving a first test case which is considered as a reference case, we study the influence of the following parameters : substrate supply θ_S, intensity on the upper surface of the water I_0, absorption coefficient τ_M and variation of light. Note that other numerical simulations are presented in appendices to show the influence of the elastic tensor coefficients γ_M and γ_E and of the maximal photosynthesis rate μ_P.

The one dimensional setting has to be interpreted as the case when biofilms have a uniform horizontal distribution and the space variable under consideration is therefore the height. In all the simulations presented here, we take the following values: the length of the domain is equal to $L_x = 5$ mm, the number of discretisation points is $N_x = 400$ and the initial data are taken as:

$$A_0 = 5 \cdot 10^{-2} \chi_{x \leqslant 10^{-4}}, \qquad N_0 = 8.38 \cdot 10^{-3} \chi_{x \leqslant 10^{-4}},$$
$$E_0 = 0, \qquad L_0 = 1 - A_0 - N_0 - E_0,$$
$$S_0 = \theta_S, \qquad C_0 = \theta_C,$$
$$O_0 = \theta_O,$$

with

$$\theta_S = 5 \cdot 10^{-5} \ \ \mathrm{kg}\mathbf{S}/\mathrm{kg}\mathbf{L}, \qquad \theta_C = 100 \cdot 10^{-5} \ \ \mathrm{kg}\mathbf{C}/\mathrm{kg}\mathbf{L},$$
$$\theta_O = 7.2 \cdot 10^{-6} \ \ \mathrm{kg}\mathbf{O}/\mathrm{kg}\mathbf{L},$$

and where $\chi_{x \leqslant 10^{-4}}$ denotes the characteristic function of interval $[0, 10^{-4}]$. Boundary conditions are described in Section 3.5; they are all homogeneous, except for the components dissolved in liquid on top of the domain (i.e. $x = L_x$), for which we take the same values θ_S, θ_C and θ_O as for initial conditions above. Values of all the other parameters of the system can be found in Table 1 and 2. Finally, light intensity on the upper surface of water ($x = L_x$) is given by $I_0(t, L_x) = I_{opt}$ and is independent of time.

4.1. First tests

Fig. 2 represents the volume fractions of the biofilm components, that is to say *A, N, E* and $A + N + E$, and the mass fractions of the components dissolved in liquid, that is to say *S, C* and *O*. These quantities are displayed for $t = 10$, 45 and 90 days. For longer times, the evolution is similar to the one observed until 90 days and no saturation effect is observed.

Note that the left boundary of the domain corresponds to the bottom of the tank and the right boundary to the top of the tank, where nutrients are brought to the domain.

We can observe the evolution of a front, corresponding to the development of biofilm within water. The total volume fraction of biofilm increases with time at the location of the front (see the purple curve of $A + N + E$ on Fig. 2(a), (c), (e)). Moreover we observe that the composition of the biofilm is not homogeneous in space: in the region of the front, the amount of microalgae **A** (in green in Fig. 2) and of **N** (in red) is particularly high, whereas the region of the bottom is almost exclusively made of extra-cellular matrix (in brown).

Now, looking at the figures displaying the mass fractions of the components dissolved in liquid, we distinguish three regions. The interpretation of these regions is tightly linked to the limiting factors involved in the reaction rates and displayed in Fig. 5, that is to say, starting from the right side of the domain:

- On top of the tank, corresponding to $x \in [2.3; 5]$ in Fig. 2(f), the mass fractions of **S** and **C** are smaller than their values on the top boundary, which are fixed by boundary conditions, owing to their consumption by the biofilm at the front: $x \in [2.2; 2.4]$, whereas the mass fraction of **O** is higher due to the significant release of oxygen by photosynthesis.
- In the area directly behind the front, corresponding to $x \in [2.0; 2.3]$ in Fig. 2(f), the mass fraction of **C** slowly increases due to release induced by respiration (see the red curve of f_R in Fig. 5(d)) and due to absence of consumption because of the null photosynthesis rate (see the orange curve of f_P in Fig. 5(c)). For oxygen, an opposite phenomenon occurs : since oxygen is no longer active, its mass fraction decreases due to respiration. In this area, substrate is slightly consumed and its mass fraction decreases slowly.
- Finally, on bottom of the tank, where biofilm is almost exclusively made of extracellular matrix, corresponding to $x \in [0; 2.0]$ in Fig. 2(f), mass fractions are nearly constant in space.

Assuming that biofilm is uniform in the two other directions, the daily production rate is estimated to 0.948 g $m^{-2}d^{-1}$ of dry matter (considering that biofilm contains about 90% of water) at $t = 10$ days, 1.087 at $t = 45$ days and 1.513 at $t = 90$ days. On average, daily production rate is equal to 1.152 g $m^{-2}d^{-1}$. This value is comparable with biological experiments made by Schnurr and Allen (2015); Schnurr et al. (2014) or Gross et al. (2013), in which daily productivity is estimated between 0.7 g $m^{-2}d^{-1}$ and 6.5 g $m^{-2}d^{-1}$ depending on conditions, species and cultivation methods.

Note that the mass fractions of components dissolved in liquid phase influence the reaction terms through the reaction rates. However, the amount of matter is given by the quantities *SL, CL* and *OL* that are represented in Fig. 3. For convenience, we only describe Fig. 3(c) but the two other figures in Fig. 3 read similarly. On top of the tank (i.e. $x \in [2.3; 5]$) the volume fraction of liquid is equal to 1 so *SL, CL* and *OL* have the same behaviour as their mass fractions *S, C* and *O*, that is to say the amount of **S** and of **C** decreases, whereas the mass fraction of **O** increases. In the biofilm front area (i.e. $x \in [2.0; 2.3]$), the volume fraction of liquid decreases suddenly, leading to a decrease of *SL, CL* and *OL*. On bottom of the tank, the amount of these quantities slowly increases along with the volume fraction of liquid.

Fig. 4 represents the velocities of the different components at t=90 days. We observe that the velocities of microalgae and of extra-cellular matrix behave similarly, that is to say they are positive around the biofilm front region, as expected from the evolution of biofilm front. Indeed, the front location, defined as the point where the gradient of $A + N + E$ is the largest, moves with a speed equal to 26.8 μm d^{-1}, which is in the range of 23–27 μm d^{-1} measured in Schnurr et al. (2014). On the opposite, the velocity of liquid is negative, which can be explained by the fact that liquid is consumed by biofilm through photosynthesis.

Now, let us illustrate in Fig. 5 the limiting factors of the mechanisms involved in biofilm development. Since all the considered mechanisms cannot take place in absence of microal-

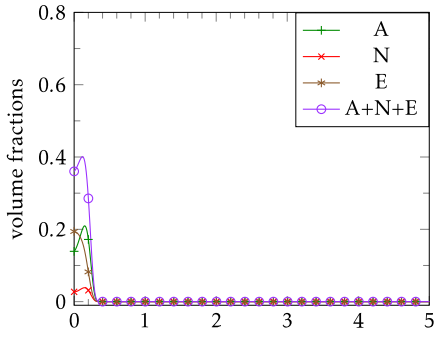

(a) Volume fraction of the different biofilm constituents at $t = 10$ days.

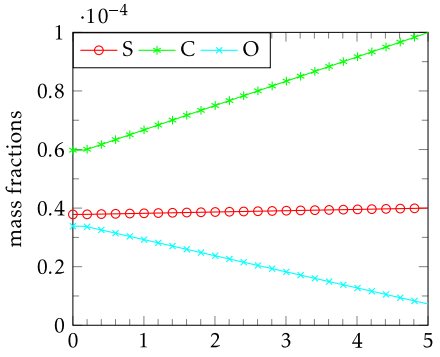

(b) Mass fraction of the different components dissolved in the liquid at $t = 10$ days.

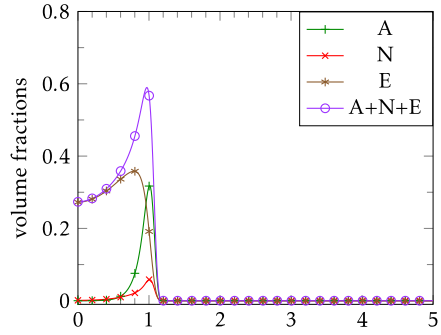

(c) Volume fraction of the different biofilm constituents at $t = 45$ days.

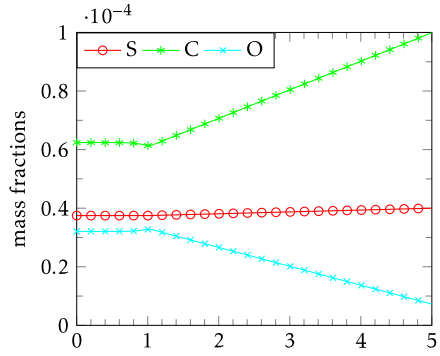

(d) Mass fraction of the different components dissolved in the liquid at $t = 45$ days.

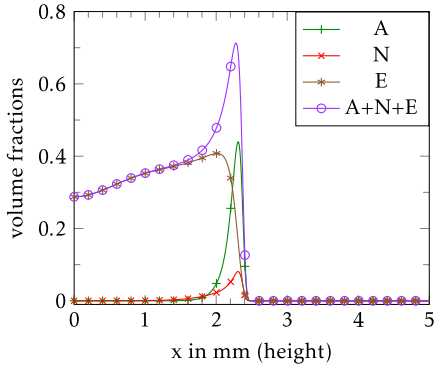

(e) Volume fraction of the different biofilm constituents at $t = 90$ days.

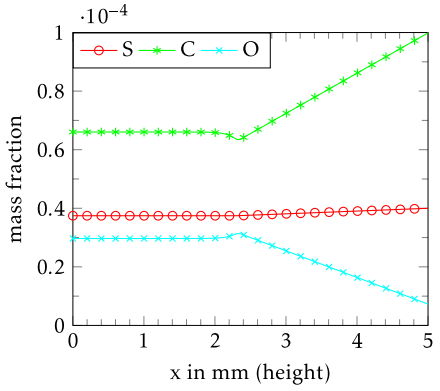

(f) Mass fraction of the different components dissolved in the liquid at $t = 90$ days.

Fig. 2. Evolution of the front of the biofilm with respect to time. The biofilm is composed mostly of algae in the front region and of extra-cellular matrix on the bottom of the tank. Plot of volume fractions of the biofilm components in subfigures 2a, 2c and 2e and mass fractions of the components dissolved in the liquid in subfigures 2b, 2d and 2f with respect to height for different times. The first row (subfigures 2a and 2b) corresponds to $t = 10$ days, the second row (subfigures 2c and 2d) corresponds to $t = 45$ days and the third row (subfigures 2e and 2f) corresponds to $t = 90$ days. The subfigures 2a, 2c and 2e of the first column represent the volume fraction of the biofilm components, namely: the pool of carbon storage (A, green), the functional biomass (N, red), the extra-cellular matrix (E, brown) and the whole biofilm (A+N+E, purple). The subfigures 2b, 2d and 2f of the second column represent the mass fraction of the components dissolved in the liquid, namely: the substrate (S, red) the carbon dioxyde (C, green) and the oxygen (O, blue).

gae, we concentrate on the biofilm region, namely for $x \in [0; 1.2 \cdot 10^{-3}]$ in Fig. 5(a) and (b) and $x \in [0; 2.4 \cdot 10^{-3}]$ in Fig. 5(c) and (d).

Figs. 5(a) and (c) represent functions f_Q, f_L, f_C, f_O and f_I described at Eqs. (12b)–(12e) and involved in the expression of the photosynthesis reaction rate (14a), evaluated at t = 45 and 90 days, respectively.

At $t = 45$ days, we can observe that elementary functions f_Q and f_C have values greater than 0.9, meaning that they are not limiting for photosynthesis. On the opposite, functions f_I, f_O and f_L take smaller values, meaning that photosynthesis is limited by the lack of light and liquid and inhibited by high concentration of oxygen. More precisely, 90% of light is absorbed in the first 240 μm after the biofilm front (i.e. $x \in \left[0.87 \cdot 10^{-3}; 1.11 \cdot 10^{-3}\right]$) leading to f_I (in yellow) equal to zero for $x \in \left[0; 0.8 \cdot 10^{-3}\right]$. On the interval $\left[0; 1.2 \cdot 10^{-3}\right]$, where oxygen concentration is high, see Fig. 2(d), the function f_O has values under 0.55, meaning that oxygen inhibits the photosynthesis process. The function f_L (in blue) rapidly decreases to 0.67 at $x = 0.97$ mm and slowly increases until 0.89.

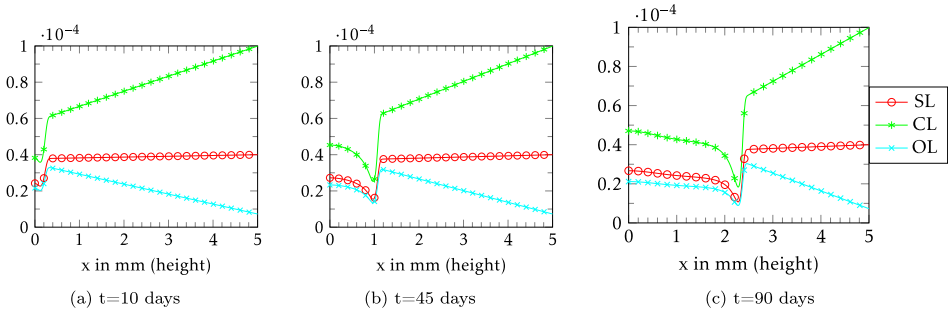

(a) t=10 days (b) t=45 days (c) t=90 days

Fig. 3. Evolution of the front of the biofilm with respect to time. Dissolved components are consumed at the biofilm front. Plot of the product between the liquid volume fraction and the mass fraction for the dissolved components, namely the substrate (SL, red) the carbon dioxyde (CL, green) and the oxygen (OL, blue) with respect to height at t=10 days in subfigure 3a, t=45 days in subfigure 3b and at t=90 days in subfigure 3c.

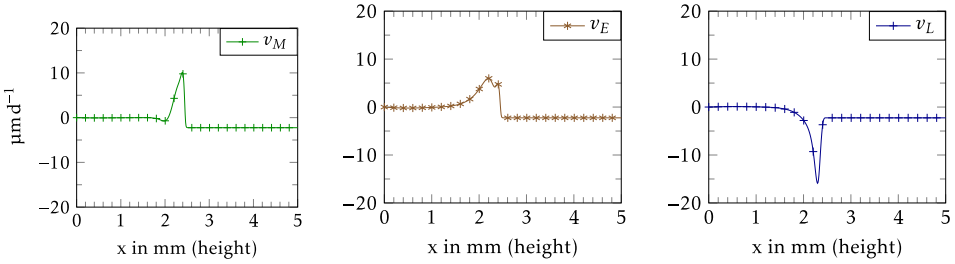

(a) Microalgae velocity (v_M) (b) ECM velocity (v_E) (c) Liquid velocity (v_L)

Fig. 4. Evolution of the front of the biofilm with respect to time. The velocities of microalgae and of extra-cellular matrix behave similarly, whereas the velocity of liquid is negative. Plot of velocities of the different components of the system with respect to height at $t = 90$ days. Subfigure 4a on the left represents the velocity v_M of the microalgae (carbon pool and functional biomass), subfigure 4b in the middle represents the velocity v_E of the extra-cellular matrix and subfigure 4c on the right represents the velocity v_L of the liquid.

So liquid is not limiting inside the biofilm but is partially limiting on the biofilm front. Finally, the product $f_P = f_Q f_L f_C f_O f_I$, which is nearly equal to the photosynthesis rate is also plotted on the same figure (in orange) and it confirms that photosynthesis takes place on top of the biofilm, that is to say in the interval $\left[1 \cdot 10^{-3}; 1.2 \cdot 10^{-3}\right]$.

At t=90 days, we observe in Fig. 5(c) that f_O is now above 0.82, meaning that oxygen concentration is somewhat inhibiting. Indeed, according to Figs. 2(d) and (f), the mass fraction of oxygen in biofilm area has slightly decreased between 45 and 90 days. At the same time, the total volume fraction of biofilm has increased (see Fig. 2(c) and (e)), leading the volume fraction of water to decrease. So, f_L takes values around 0.6 in the area of the biofilm front and water becomes limiting. For the light intensity and the effect of the quota of the functional biomass, we observe the same effects as at t=45 days: 90% of the light is absorbed in the first 250 μm after the biofilm front (see f_I in yellow) and Q is not limiting inside the biofilm. Finally, we also plot f_P, that confirms that photosynthesis still takes place on top of the biofilm (in the interval $\left[2.2 \cdot 10^{-3}; 2.4 \cdot 10^{-3}\right]$), even if the order of influence of the elementary functions has changed.

Now, in Figs. 5(b) and (d), we show the other functions used to compute the reactions rates (14). First, we notice that Fig. 5(d) is basically a shift of Fig. 5(b) meaning that the influence of f_R, f_S, f_N and f_D, unlike the elementary functions that compose φ_P, does not change inside the biofilm over time. We can also observe that the graph of f_R, defined by $f_R(O) = O/(\mathcal{K}_O + O)$ and used in respiration rate (14b), remains close to 0.96 in the biofilm area, so oxygen is almost not limiting for respiration. Then, concerning the functional biomass synthesis rate (14c), function $f_S(S) = S/(\mathcal{K}_S + S)$ is nearly equal to 1, whereas function $f_N(Q) = \max\{Q_{max} - \max\{Q, Q_{min}\}\}/(Q_{max} - Q_{min})$ vanishes in the biofilm region. Therefore, functional biomass synthesis happens mostly in the region of the biofilm front. Finally $f_D(O) = 1 - \beta\hat{O}/\left(\hat{O}^\beta + \beta - 1\right)$ with $\hat{O} = O/O_{ref}$, present in death rates (14g), takes higher values in the biofilm, since the presence of oxygen increases these rates.

4.2. Influence of the value of substrate supply θ_S

We study in this subsection the influence of the value of substrate supply θ_S.

Fig. 6(a) represents the average daily production rate (estimated on 90 days) of dry biomass for the different constituents of the biofilm with respect to the parameter θ_S. According to this graph, the daily production rate of dry biofilm ($\mathbf{A} + \mathbf{N} + \mathbf{E}$) increases until $\theta_S = 1.5$ μg**S**/g**L**, to reach 1.21 g m^{-2}d^{-1} and then slowly decreases. However, differences can be observed between the production rate of each component. Indeed the production rates of carbon pool (**A**) and functional biomass (**N**) increase linearly until $\theta_S = 2.5$ μg**S**/g**L**; then they stabilise at 90.2 mg m^{-2}d^{-1} for **A** and 29.2 mg m^{-2}d^{-1} for **N**. Behaviour of ECM is different: its production rate increases until 1.14 g m^{-2}d^{-1} for $\theta_S = 1.5$ μg**S**/g**L**, then decreases and stabilises at 1.08 for $\theta_S > 2.5$ μg**S**/g**L**. These changes of production rate impact the biofilm composition, as it can be observed in Fig. 6(b). Indeed, from $\theta_S = 0$ to $\theta_S = 2.5$ μg**S**/g**L**, the percentage of EPS composing the biofilm decreases from 93.6 to 86.3%, whereas the percentage of carbon pool (resp. functional biomass) increases from 5.7 to 10.8% (resp. 0.7 to 2.9%). Then, for $\theta_S > 2.5$ μg**S**/g**L**, the biofilm composition remains stable. The front velocity behaves as the total production rate, namely it increases until $\theta_S = 1.5$ μg**S**/g**L** to reach 31.6 μm d^{-1} and then slowly decreases until 26.1 μm d^{-1}.

In order to better understand the influence of substrate supply, we present the results of numerical simulations performed with $\theta_S = 1.5 \cdot 10^{-6}$; the other parameters remain unchanged. Fig. 7 represents volume and mass fractions at $t = 90$ days and in Fig. 8, we plot the elementary functions that compose the reaction rates.

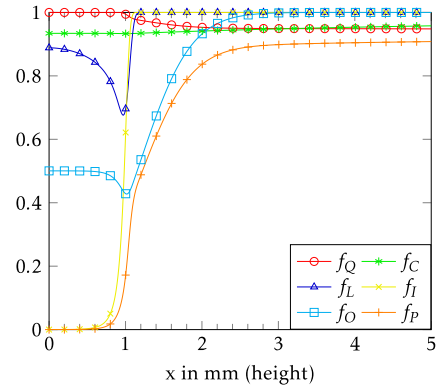

(a) Elementary functions (12) that compose the photosynthesis rate (14a) at t=45 days.

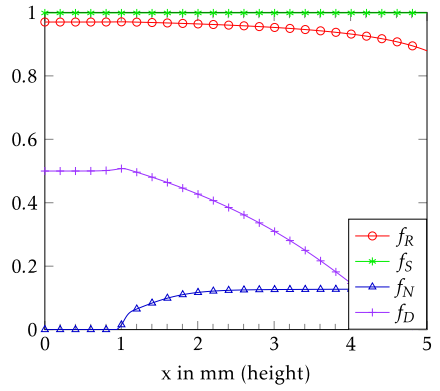

(b) Other elementary functions that compose the other reaction rates (14) at t=45 days.

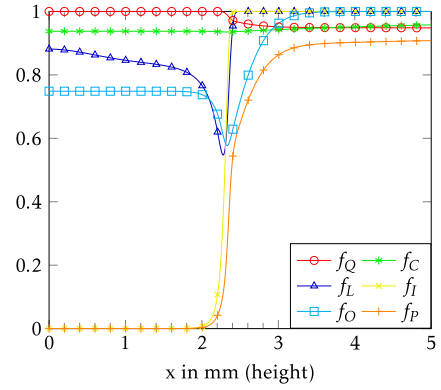

(c) Elementary functions (12) that compose the photosynthesis rate (14a) at t=90 days.

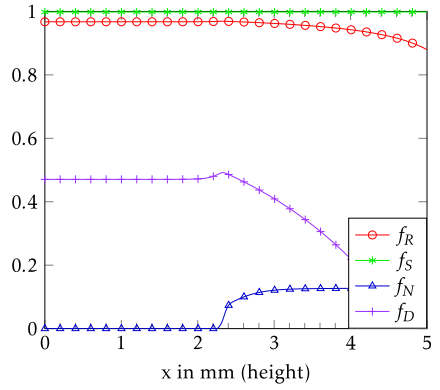

(d) Other elementary functions that compose the other reaction rates (14) at t=90 days.

Fig. 5. Evolution of the front of the biofilm with respect to time. Photosynthesis is limited by the lack of light and liquid and inhibited by high concentration of oxygen. Plot of elementary functions that compose the photosynthesis rate in subfigures 5a and 5c (left column) and other elementary functions that compose the reactions rates of respiration, functional biomass synthesis, extracellular matrix excretion and death in subfigures 5b and 5d (right column), for t=45 days (5a and 5b, i.e.: first row) and t=90 days (5c and 5d, i.e.: second row). Subfigures 5a and 5c show the functions that compose the photosynthesis rate (14a), namely $f_Q(Q_{max}-Q_{min})/Q_{max} = \max\{0, 1-Q_{min}/\min\{Q, Q_{max}\}\}$ in red (12b), $f_C(C) = C/(\mathcal{K}_C + C)$ in green (12c), $f_L(L) = (\mathcal{K}_L+1)L/(\mathcal{K}_L+L)$ in night blue (12c), $f_I(I) = 2(1+\mathcal{K}_I)\hat{I}/\left(\hat{I}^2 + 2\mathcal{K}_I\hat{I}+1\right)$ with $\hat{I} = I/I_{opt}$ in yellow (12e), $f_O(O) = 1/\left(1+(O/\mathcal{K}_O)^\alpha\right)$ in cyan (12d) and $f_P = f_Q\ f_C\ F_L\ F_I\ f_O(Q_{max}-Q_{min})/Q_{max}$ in orange. The elementary functions in subfigures 5(b) and 5(d) are $f_R(O) = O/(\mathcal{K}_O + O)$ present in the respiration rate (14b), $f_S(S) = S/(\mathcal{K}_S + S)$ and $f_N(Q) = \max\{Q_{max} - \max\{Q, Q_{min}\}\}/(Q_{max}-Q_{min})$ present in the functional biomass synthesis rate (14c) and $f_D(O) = 1-\beta\hat{O}/\left(\hat{O}^\beta + \beta - 1\right)$, with $\hat{O} = O/O_{ref}$, present in the death rates (14g) and (14h).

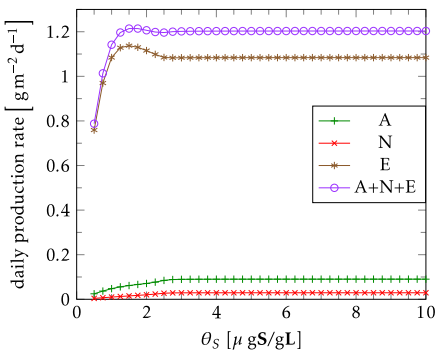

(a) Average production rate of biofilm constituents with respect to substrate supply θ_S. In this figure we display the production rate of carbon pool (A, green), functional biomass (N, red), extracellular matrix (E, brown) and of the whole biofilm (A+N+E, purple).

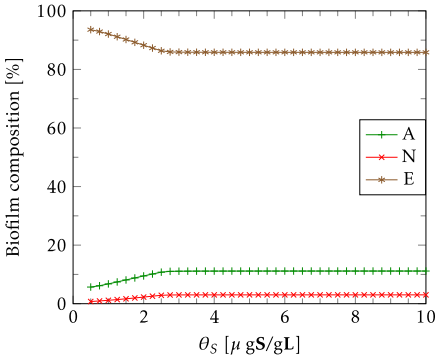

(b) Mass of biofilm constituents as a percentage of the total biofilm mass at t=90 days with respect to substrate supply θ_S. In this figure we display the percentage in mass of carbon pool (A, green), functional biomass (N, red) and extra-cellular matrix (E, brown).

Fig. 6. Influence of the value of substrate supply θ_S. EPS production rate increases more rapidly than carbon pool and functional biomass for small values of θ_S. For larger values of θ_S, the production rates reach some thresholds. Plot of average production rate of dry biofilm constituent in subfigure 6a (left) and biofilm composition in subfigure 6b (right) at t=90 days with respect to substrate supply θ_S.

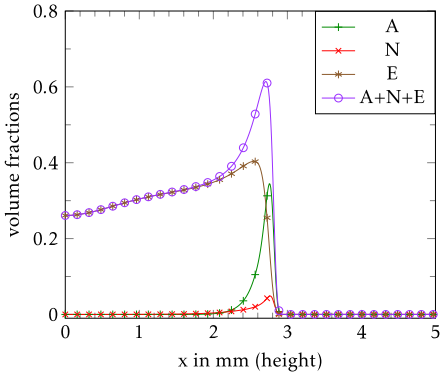

(a) Volume fraction of the different biofilm constituents with respect to height at $t = 90$ days, in the case of substrate deficiency. This figure shows the volume fraction of the pool of carbon storage (A, green), the functional biomass (N, red), the extra-cellular matrix (E, brown) and the whole biofilm (A+N+E, purple).

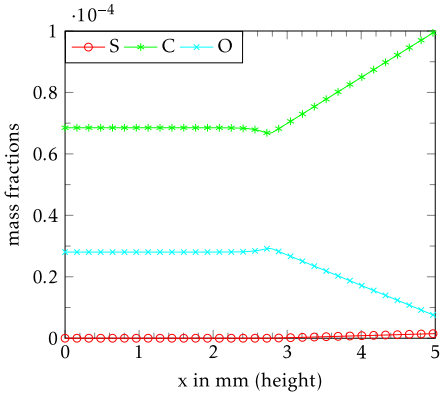

(b) Mass fraction of the different components dissolved in the liquid with respect to height at $t = 90$ days, in the case of substrate deficiency. This figure shows the substrate (S, red), the carbon dioxyde (C, green) and the oxygen (O, blue).

Fig. 7. Influence of the value of substrate supply θ_S. Substrate deficiency promoting extra-cellular matrix excretion. Plot of volume fraction of the biofilm components in subfigure 7a (left), and mass fraction of the components dissolved in the liquid in subfigures 7b (right), with respect to height at t=90 days in the case of substrate deficiency.

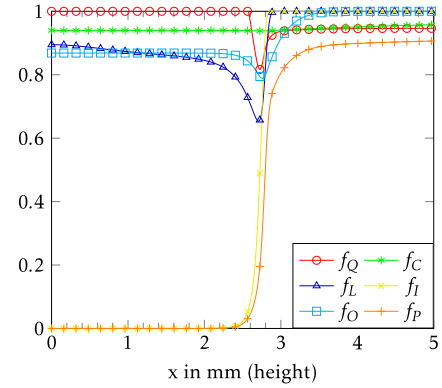

(a) Elementary functions (12) that compose the photosynthesis rate (14a) at t=90 days in the case of substrate deficiency, that is to say $f_Q\,(Q_{max}-Q_{min})/Q_{max} = \max\{0, 1-Q_{min}/\min\{Q,Q_{max}\}\}$ in red (12b), $f_C(C) = C/(\mathcal{K}_C + C)$ in green (12c), $f_L(L) = (\mathcal{K}_L+1)\,L/(\mathcal{K}_L+L)$ in night blue (12c), $f_I(I) = 2\,(1+\mathcal{K}_I)\,\hat{I}/\left(\hat{I}^2+2\mathcal{K}_I\hat{I}+1\right)$ with $\hat{I} = I/I_{opt}$ in yellow (12e), $f_O(O) = 1/(1+(O/\mathcal{K}_O)^\alpha)$ in cyan (12d) and $f_P = f_Q\,f_C\,F_L\,F_I\,f_O\,(Q_{max}-Q_{min})/Q_{max}$ in orange.

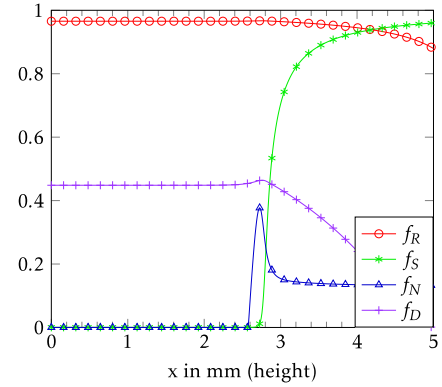

(b) Other elementary functions that compose the other reaction rates (14) at t=90 days in the case of substrate deficiency. The functions are $f_R(O) = O/(\mathcal{K}_O+O)$ present in the respiration rate (14b), $f_S(S) = S/(\mathcal{K}_S+S)$ and $f_N(Q) = \max\{Q_{max}-\max\{Q,Q_{min}\}\}/(Q_{max}-Q_{min})$ present in the functional biomass synthesis rate (14c) and $f_D(O) = 1-\beta\hat{O}/\left(\hat{O}^\beta+\beta-1\right)$, with $\hat{O} = O/O_{ref}$, present in the death rates (14g) and (14h).

Fig. 8. Influence of the value of substrate supply θ_S. Photosynthesis rate is higher than in previous simulations. Plot of elementary functions that compose the photosynthesis rate in subfigure 8a (left) and other elementary functions that compose the reactions rates of respiration, functional biomass synthesis, extracellular matrix excretion and death in subfigure 8b (right), for t=90 days in the case of substrate deficiency.

We remark that these parameters lead to a substrate deficiency, since mass fraction S (in red in Fig. 7(b)) is equal to zero in the biofilm region. Substrate deficiency promotes extra-cellular matrix excretion: the volume fraction of the whole biofilm is almost the same as previously, with a difference of less than 1.2%, but the shape and the composition change significantly. The pool of carbon storage and the functional biomass volume fractions are 19.9% and 38.0% smaller, while the ECM volume fraction is 9.8% larger, see Figs. 7(a) and 2(e). Moreover, the front of the biofilm has reached 2.8 µm instead of 2.4 µm and the peak on the biofilm front is smaller.

Regarding the elementary functions that compose the reaction rates, we notice that the photosynthesis rate is higher than in previous simulations, see Fig. 8(a). Indeed the photosynthesis is less limited by the excess of oxygen and the lack of liquid according to f_O and $f+L$, respectively. Moreover, the functional biomass synthesis rate (14c) is influenced by function $f_S(S) = S/(\mathcal{K}_S+S)$, which is nearly equal to zero in Fig. 8(a) inside the biofilm region $x \in [0;\ 2.75]$ mm. This effect is compensated by the functional biomass quota Q through the function $f_N(Q) = \max\left\{\frac{Q_{lim}-\max\{Q,Q_{\min}\}}{Q_{lim}-Q_{\min}}\right\}$, which is non zero above 2.6 mm (instead of 2.3 mm in Fig. 5(d)). In addition, f_N takes larger values at the biofilm front: 0.37 instead of 0.1.

4.3. *Influence of light intensity on the upper surface of water:* I_0(t, L_x)

In this subsection, we investigate the influence of light intensity on the average daily production rate and on the velocity of the biofilm front.

Fig. 9(a) represents the average daily production rate (estimated on 90 days) of dry biomass for the different constituents of the biofilm with respect to the light intensity on the upper surface $I_0(t, L_x)$. We can observe that the average production rate for **A, N** and **E** increases until $I_0(t, L_x) = I_{opt}$ and then decreases. So the maximal productivity is reached for $I_0(t, L_x) = I_{opt}$, whereas I_{opt} is the light intensity for which f_I is maximal in the photosynthesis rate. We

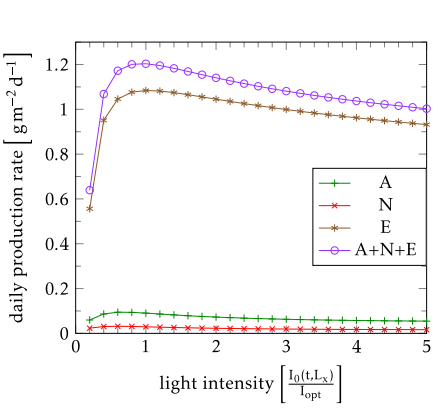

(a) Average production rate of biofilm constituents during 90 days with respect to light intensity on the upper surface of water. In this figure we display the production rate of carbon pool (A, green), functional biomass (N, red), extra-cellular matrix (E, brown) and of the whole biofilm (A+N+E, purple).

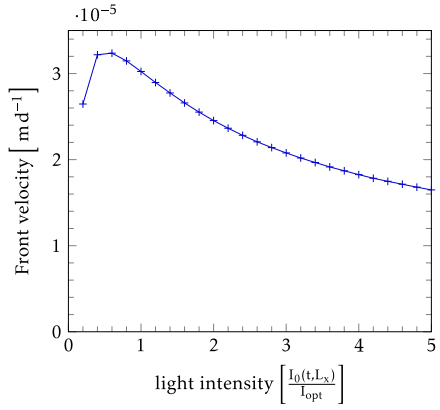

(b) Average velocity of the biofilm front during 90 days with respect to light intensity on the upper surface of water.

Fig. 9. Influence of light intensity on the upper surface of water. Average production rates for **A, N** and **E** increase until $I_0(t, L_x) = I_{opt}$ and then decrease. Plot of average daily production rate of biofilms constituents in subfigure 9a and of average velocity of the biofilm front in subfigure 9b during 90 days.

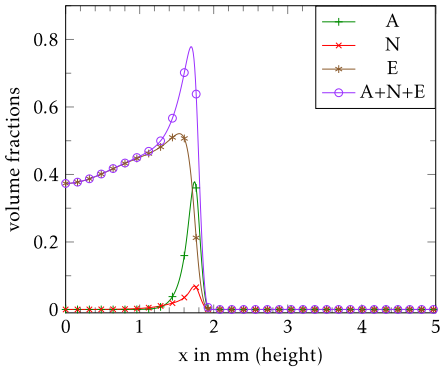

(a) Volume fraction of the different biofilm constituents with respect to height at $t = 90$ days, when the light intensity on the upper surface of water is set to $I_0(t, L_x) = 3I_{opt}$. This figure shows the pool of carbon storage (A, green), the functional biomass (N, red), the extra-cellular matrix (E, brown) and the whole biofilm (A+N+E, purple).

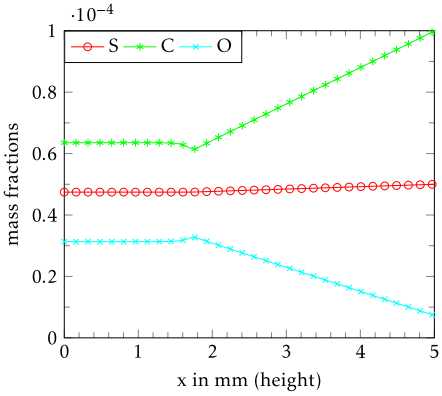

(b) Mass fraction of the different components dissolved in the liquid with respect to height at t=90 days, when the light intensity on the upper surface of water is set to $I_0(t, L_x) = 3I_{opt}$. This figure shows the substrate (S, red), the carbon dioxyde (C, green) and the oxygen (O, blue).

Fig. 10. Influence of light intensity on the upper surface of water. In the biofilm region, mass fraction of inorganic carbon is smaller than before whereas mass fraction of oxygen is greater. Plot of volume fraction of the biofilm components in subfigure 10a (left), and mass fraction of the components dissolved in the liquid in subfigures 10b (right), with respect to height at t=90 days, when the light intensity on the upper surface of water is set to $I_0(t, L_x) = 3I_{opt}$.

can also observe that all the biofilms components (**A, N** and **E**) behave similarly. Now, Fig. 9(b) shows that the velocity of the biofilm front is maximal for $I_0(t, L_x) = 0.6I_{opt}$, that is to say the maximal daily production rate and the maximal velocity of the front are not reached for the same values of $I_0(t, L_x)$.

As we can remark in Fig. 10, for a light intensity on the upper surface $I_0(t, L_x) = 3I_{opt}$, shape of the biofilm components (**A, N, E**) and mass fraction of the substrate (**S**) are comparable to the case when $I_0(t, L_x) = I_{opt}$, represented in Fig. 2(e) and (f). But in the biofilm region, for a higher value of light intensity, mass fraction of inorganic carbon is smaller whereas mass fraction of oxygen is greater.

The curves that represent in Fig. 11(b) the elementary functions used in the reaction rates differ also partly, especially f_I. Outside of the biofilm region, namely $x \in [1.9 \cdot 10^{-3}; 5 \cdot 10^{-3}]$, the value of f_I is about 0.62, meaning that if microalgae were present in this area, photosynthesis would be inhibited due to a too high light intensity. Then, gradually, as light penetrates into the biofilm and is absorbed, its intensity decreases until it reaches the optimal light intensity, here for $x = 1.76$ mm. Finally, as light intensity continues to be absorbed and thus decreases, f_I decreases until it reaches 0 for $x \sim 1.5$ mm. We can also observe that f_O takes smaller values in the area of the biofilm front, when the light intensity on the upper surface is higher.

4.4. Influence of light absorption coefficient for the biofilm τ_M

In this subsection, we investigate the influence of the light absorption coefficient of microalgae τ_M, see equation (13), which accounts directly for the light penetration in the biofilm. In Fig. 12 we represent the volume and mass fractions for the constituents considered in the model with the light absorption parameter of microalgae set to $\tau_M = 1.25 \cdot 10^4$ m^{-1}, i.e. twice smaller than the simulations of Section 4.1. Although the result remains consistent with those presented in the first test case, see Fig. 2(e), we can observe a few differences. Indeed after 90 days, the volume fraction of **A** (in green) is 1.1% larger and the volume fraction of ECM (in brown) is 3.5% larger, whereas the volume fraction of func-

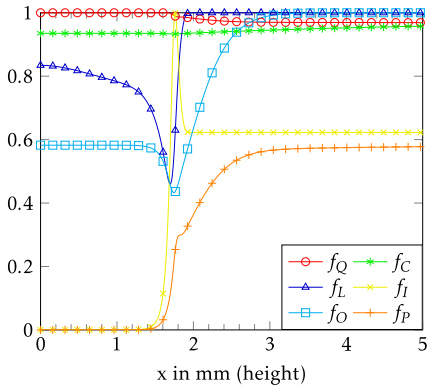

(a) Elementary functions (12) that compose the photosynthesis rate (14a) at t=90 days when the light intensity on the upper surface of water is set to $I_0(t, L_x) = 3I_{opt}$, that is to say $f_Q\,(Q_{max} - Q_{min})\,/Q_{max} = \max\{0, 1 - Q_{min}/\min\{Q, Q_{max}\}\}$ in red (12b), $f_C(C) = C/(\mathcal{K}_C + C)$ in green (12c), $f_L(L) = (\mathcal{K}_L + 1)\,L/(\mathcal{K}_L + L)$ in night blue (12c), $f_I(I) = 2\,(1 + \mathcal{K}_I)\,\hat{I}/\left(\hat{I}^2 + 2\mathcal{K}_I\hat{I} + 1\right)$ with $\hat{I} = I/I_{opt}$ in yellow (12e), $f_O(O) = 1/(1 + (O/\mathcal{K}_O)^\alpha)$ in cyan (12d) and $f_P = f_Q\,f_C\,F_L\,F_I\,f_O\,(Q_{max} - Q_{min})\,/Q_{max}$ in orange.

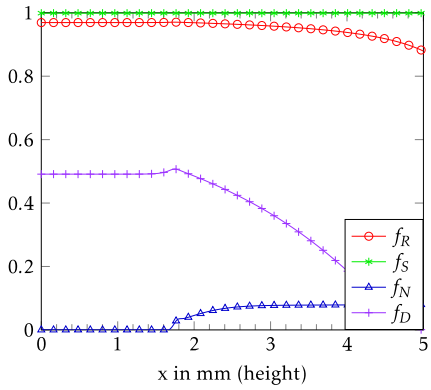

(b) Other elementary functions that compose the other reaction rates (14) at t=90 days and when the light intensity on the upper surface of water is set to $I_0(t, L_x) = 3I_{opt}$. The functions are $f_R(O) = O/(\mathcal{K}_O + O)$ present in the respiration rate (14b), $f_S(S) = S/(\mathcal{K}_S + S)$ and $f_N(Q) = \max\{Q_{max} - \max\{Q, Q_{min}\}\}\,/\,(Q_{max} - Q_{min})$ present in the functional biomass synthesis rate (14c) and $f_D(O) = 1 - \beta\hat{O}/\left(\hat{O}^\beta + \beta - 1\right)$, with $\hat{O} = O/O_{ref}$, present in the death rates (14g) and (14h).

Fig. 11. Influence of light intensity on the upper surface of water. Gradually, as light penetrates into the biofilm and is absorbed, its intensity decreases until it reaches the optimal light intensity. Plot of elementary functions that compose the photosynthesis rate in subfigure 11a (left) and other elementary functions that compose the reactions rates of respiration, functional biomass synthesis, extracellular matrix excretion and death in subfigure 11b (right), for t=90 days and when the light intensity on the upper surface of water is set to $I_0(t, L_x) = 3I_{opt}$.

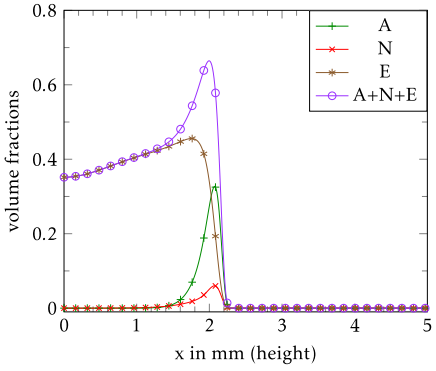

(a) Volume fraction of the different biofilm constituents with respect to height at $t = 90$ days when the light absorption coefficient is decreased to $\tau_M = 1.25 \cdot 10^4$ m^{-1}. This figure shows the pool of carbon storage (A, green), the functional biomass (N, red), the extra-cellular matrix (E, brown) and the whole biofilm (A+N+E, purple).

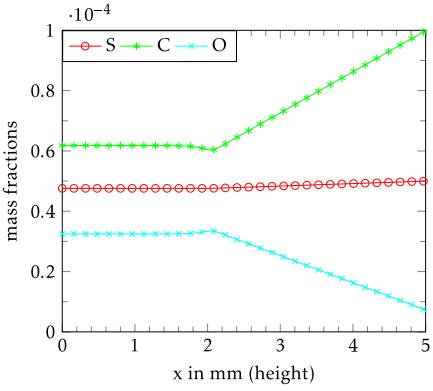

(b) Mass fraction of the different components dissolved in the liquid with respect to height at $t = 90$ days when the light absorption coefficient is decreased to $\tau_M = 1.25 \cdot 10^4$ m^{-1}. This figure shows the substrate (S, red), the carbon dioxyde (C, green) and the oxygen (O, blue).

Fig. 12. Influence of light absorption coefficient τ_M. Increase of volume fractions of carbon pool and ECM and decrease of functional biomass, leading to a decrease of total mass of the biofilm. Plot of volume fraction of the biofilm components in subfigure 12a (left), and mass fraction of the components dissolved in the liquid in subfigures 12b (right), with respect to height at t=90 days and when the light absorption coefficient is decreased to $\tau_M = 1.25 \cdot 10^4$ m^{-1}.

tional biomass (in red) is 16.3% smaller. These discrepancies lead to a decrease of less than 0.7% for the total mass of the biofilm. In Fig. 12(a), we can also notice that the biofilm front has only reached $x = 2.15$ mm whereas in the first test case in Fig. 2(e), it has reached $x = 2.37$ mm, meaning that the velocity of the biofilm front is smaller. Indeed, the front velocity is estimated to 24.1 μm d^{-1}, instead of 26.8 μm d^{-1} in Section 4.1, so the light absorption parameter has an indirect impact on the front velocity.

As regards the components dissolved in liquid represented in Fig. 12(b), we can observe that, in the biofilm area, mass fraction for carbon dioxyde is lower while oxygen mass fraction is higher compared to Fig. 2(f).

In order to explain these differences, let us take a look at the elementary functions used to build the reaction rates and represented in Fig. 13. Although light intensity through function f_I remains the main limiting parameter, it decreases more smoothly as it penetrates into the biofilm. Moreover we can observe that f_O (in cyan) takes values below 0.4 in the area of the biofilm front, so photosynthesis is here inhibited by the excess of oxygen. We can also notice that the function f_P (in orange), which is nearly the photosynthesis rate, decreases more smoothly, so photosynthesis occurs deeper into the biofilm. Regarding the other elementary functions used to build the reaction rates and represented in Fig. 13(b), only f_N has a different shape: like photosynthesis, assimilation of substrate continues to occur deeper into the biofilm.

4.5. Influence of variation of light

Finally, we consider that light intensity on top of the domain depends on time as follows:

$$I_0(t, L_x) = 3I_{opt}\max\{0, \sin(2\pi t)\},$$

such that the biofilm is periodically enlightened with an intensity between 0 and $3I_{opt}$. Results can be observed in Fig. 14 for

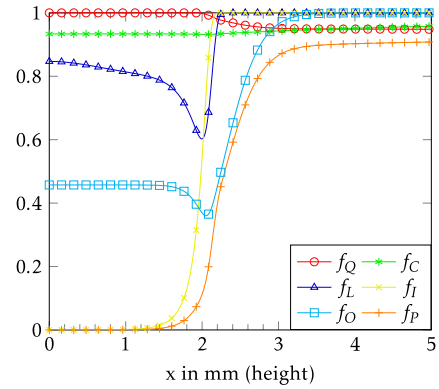

(a) Plot of elementary functions (12) that compose the photosynthesis rate (14a) at t=90 days when the light absorption coefficient is decreased to $\tau_M = 1.25 \cdot 10^4$ m^{-1}, that is to say $f_Q\,(Q_{max} - Q_{min})\,/Q_{max} = \max\{0, 1 - Q_{min}/\min\{Q, Q_{max}\}\}$ in red (12b), $f_C(C) = C/(\mathcal{K}_C + C)$ in green (12c), $f_L(L) = (\mathcal{K}_L + 1)\,L/(\mathcal{K}_L + L)$ in night blue (12c), $f_I(I) = 2\,(1 + \mathcal{K}_I)\,\hat{I}/\left(\hat{I}^2 + 2\mathcal{K}_I\hat{I} + 1\right)$ with $\hat{I} = I/I_{opt}$ in yellow (12e), $f_O(O) = 1/(1 + (O/\mathcal{K}_O)^{\alpha})$ in cyan (12d) and $f_P = f_Q\,f_C\,F_L\,F_I\,f_O\,(Q_{max} - Q_{min})\,/Q_{max}$ in orange.

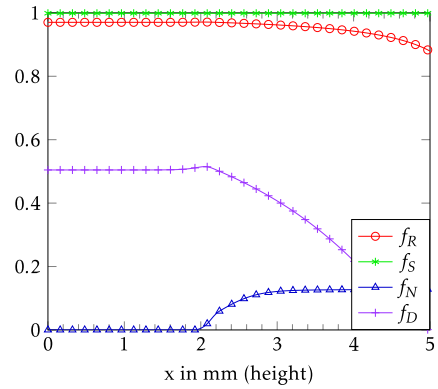

(b) Other elementary functions that compose the other reaction rates (14) at t=90 days when the light absorption coefficient is decreased to $\tau_M = 1.25 \cdot 10^4$ m^{-1}. The functions are $f_R(O) = O/(\mathcal{K}_O + O)$ present in the respiration rate (14b), $f_S(S) = S/(\mathcal{K}_S + S)$ and $f_N(Q) = \max\{Q_{max} - \max\{Q, Q_{min}\}\}\,/\,(Q_{max} - Q_{min})$ present in the functional biomass synthesis rate (14c) and $f_D(O) = 1 - \beta\hat{O}/\left(\hat{O}^{\beta} + \beta - 1\right)$, with $\hat{O} = O/O_{ref}$, present in the death rates (14g) and (14h).

Fig. 13. Influence of light absorption coefficient τ_M. Light intensity (see function f_I) remains the main limiting parameter, but its decrease as it penetrates into the biofilm is slower. Elementary functions that compose the photosynthesis rate in subfigure 13a (left) and other elementary functions that compose the reactions rates of respiration, functional biomass synthesis, extracellular matrix excretion and death in subfigure 13b (right), for t=90 days and when the light absorption coefficient is decreased to $\tau_M = 1.25 \cdot 10^4$ m^{-1}.

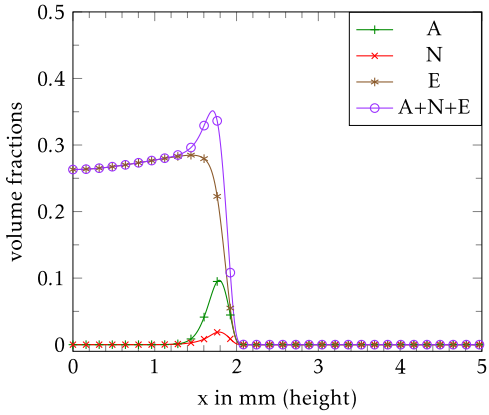

Fig. 14. Influence of variation of light. Average daily production rate over the first 150 days is equal to 0.393 g m^{-2}d^{-1} and the biofilm front moves with a speed equal to 12.4 μm d^{-1}. Plot of volume fraction of the different biofilm constituents with respect to height at $t = 150$ days, when the biofilm is periodically enlightened. This figure shows the pool of carbon storage (A, green), the functional biomass (N, red), the extra-cellular matrix (E, brown) and the whole biofilm (A+N+E, purple). (For interpretation of the references to colour in this figure legend, the reader is referred to the web version of this article.)

the volume fractions and in Figs. 15 and 16 for the mass fractions and the elementary functions that compose the reaction rates. Average daily production rate over the first 150 days is equal to 0.393 g m^{-2}d^{-1} and the biofilm front moves with a speed equal to 12.4 μm d^{-1}. Volume fractions and composition of the biofilm are unchanged. However the mass fractions of the components dissolved into liquid phase (substrate, inorganic carbon and oxygen) represented in Fig. 15 and 16 evolve all day long with the enlightenment of the biofilm. Indeed, assimilation of inorganic carbon and release of oxygen are tightly linked to photosynthesis and so to light intensity. Regarding the elementary functions that compose the photosynthesis rate and displayed in the middle column in Fig. 15 and 16, we can observe that the limiting factors are light intensity f_I and oxygen excess f_O defined in equations (12e) and (12d) respectively. As long as light intensity increases and remains smaller than I_{opt}, the photosynthesis rate on the biofilm front increases; then, when light intensity becomes greater than I_{opt}, it starts to inhibit photosynthesis on the front but enables microalgae to make photosynthesis behind the front (i.e.: $x \in [2.6; 3]$). At the same time, oxygen saturation increases due to the released induced photosynthesis and leads to an inhibition of photosynthesis; this phenomenon is confirmed by the curve of f_O in Fig. 16(b) and 16(f) that takes small values in the area of the biofilm front.

On the last column of Fig. 15 and 16, we represent the other elementary functions: $f_R(O) = O/(\mathcal{K}_O + O)$ present in the respiration rate (14b), functions $f_S(S) = S/(\mathcal{K}_S + S)$ and

$$f_N(Q) = \max\{Q_{max} - \max\{Q, Q_{min}\}\}/(Q_{max} - Q_{min})$$

present in the functional biomass synthesis rate (14c) and $f_D(O) = 1 - \beta\hat{O}/\left(\hat{O}^{\beta} + \beta - 1\right)$, with $\hat{O} = O/O_{ref}$, present in the death rates (14g) and (14h). In this simulation, substrate supply is in excess which is confirmed by the values of f_S that remain close to 1. During night (first row in Fig. 15 and 16), in the biofilm area, f_D takes values around 0.2 meaning there is death induced by lack of oxygen. The deficiency of oxygen is caused by the respiration process, represented by f_R which is equal to about 0.2 in the biofilm area. Moreover, oxygen concentration increases with the light intensity which induces f_R to increase: in the biofilm area, f_R goes from 0.2 for $I_0(t, L_x) = 0$ to 0.8 when $I_0(t, L_x) = 3I_{opt}$. Finally, we notice that the death process (see the curve of f_D) which increases with the oxygen concentration, so it is minimal for $I_0(t, L_x) = I_{opt}/2$ and it increases up to 0.2 for $I_0(t, L_x) = 3I_{opt}$.

5. Conclusion

In this paper, we have proposed a new mixture model for the growth of microalgae biofilms producing lipids. The main originality of this model is the accurate description of the physiological mechanisms involved in the formation and development combined with the use of partial differential equations for representing spatial variations of the biofilm. In particular, we use Droop's theory to describe the assimilation of carbon through photosynthesis and we represent functional biomass growth and mortality, EPS excretion process and diffusion of nutrients into the biofilm. The general form of our model is the same as in Clarelli et al. (2013), but

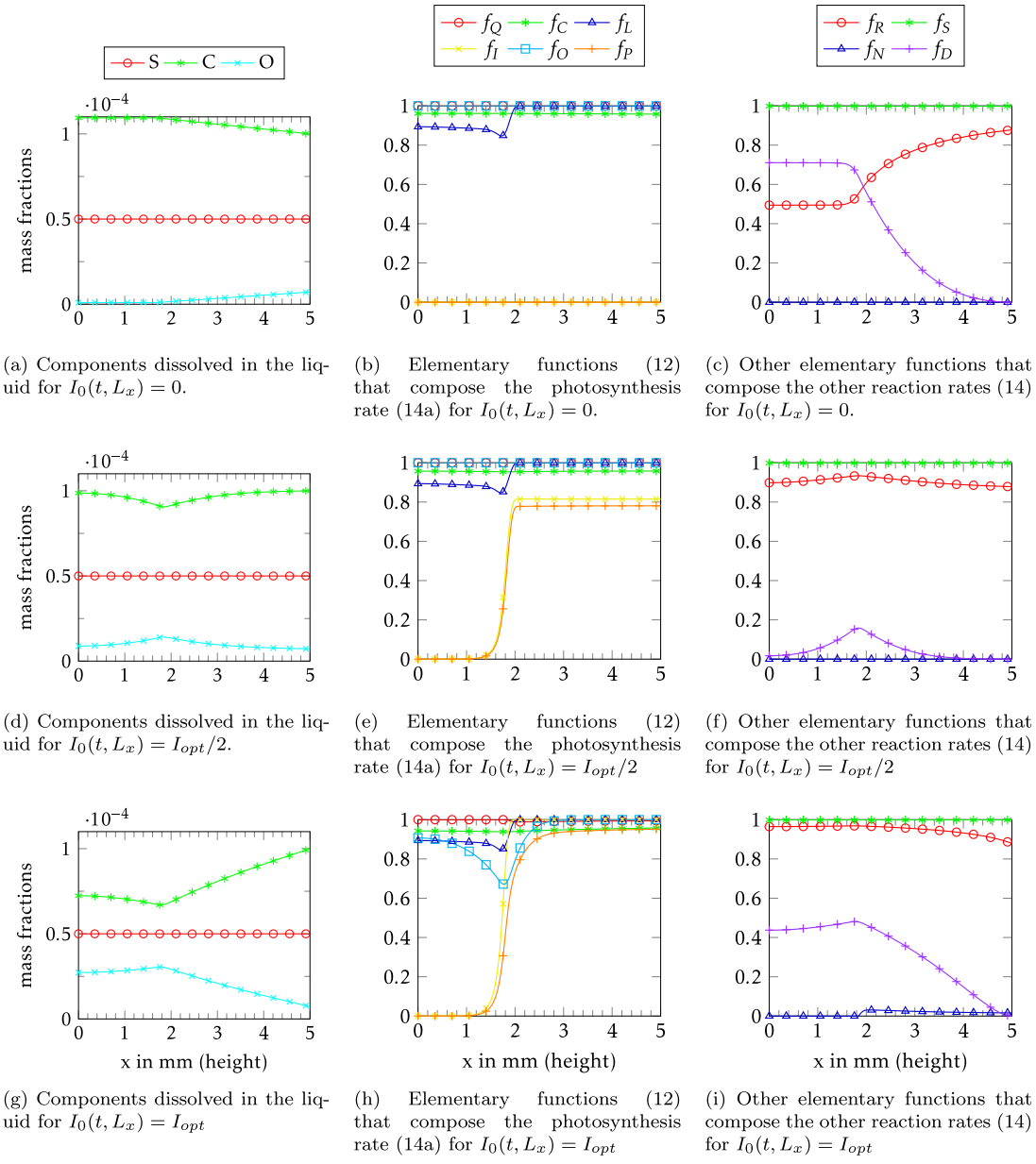

(a) Components dissolved in the liquid for $I_0(t, L_x) = 0$.

(b) Elementary functions (12) that compose the photosynthesis rate (14a) for $I_0(t, L_x) = 0$.

(c) Other elementary functions that compose the other reaction rates (14) for $I_0(t, L_x) = 0$.

(d) Components dissolved in the liquid for $I_0(t, L_x) = I_{opt}/2$.

(e) Elementary functions (12) that compose the photosynthesis rate (14a) for $I_0(t, L_x) = I_{opt}/2$

(f) Other elementary functions that compose the other reaction rates (14) for $I_0(t, L_x) = I_{opt}/2$

(g) Components dissolved in the liquid for $I_0(t, L_x) = I_{opt}$

(h) Elementary functions (12) that compose the photosynthesis rate (14a) for $I_0(t, L_x) = I_{opt}$

(i) Other elementary functions that compose the other reaction rates (14) for $I_0(t, L_x) = I_{opt}$

Fig. 15. Influence of variation of light. Deficiency of oxygen caused by the respiration process. Numerical results at t=150 days when the biofilm is periodically enlightened. Each row corresponds to a different value for the light intensity on the upper surface: in the first row which corresponds to subfigures 15a, 15b and 15c $I_0(t, L_x) = 0$, in the second row which corresponds to subfigures 15d, 15e and 15f $I_0(t, L_x) = I_{opt}/2$ and in the third row which corresponds to subfigures 15g, 15h and 15i $I_0(t, L_x) = I_{opt}$. The left column, namely subfigures 15a, 15g and 15g, shows the mass fractions of the components dissolved in the liquid. On each of these figures are represented the substrate (S, red), the carbon dioxyde (C, green) and the oxygen (O, blue). The middle column, namely subfigures 15b, 15e and 15h, shows the functions that compose the photosynthesis rate (14a). On each of these figures are represented $f_Q(Q_{max} - Q_{min})/Q_{max} = \max\{0, 1 - Q_{min}/\min\{Q, Q_{max}\}\}$ in red (12b), $f_C(C) = C/(\mathcal{K}_C + C)$ in green (12c), $f_L(L) = (\mathcal{K}_L + 1)L/(\mathcal{K}_L + L)$ in night blue (12c), $f_I(I) = 2(1 + \mathcal{K}_I)\hat{I}/\left(\hat{I}^2 + 2\mathcal{K}_I\hat{I} + 1\right)$ with $\hat{I} = I/I_{opt}$ in yellow (12e), $f_O(O) = 1/\left(1 + (O/\mathcal{K}_O)^\alpha\right)$ in cyan (12d) and $f_P = f_Q\ f_C\ F_L\ F_I\ f_O(Q_{max} - Q_{min})/Q_{max}$ in orange. The third column, namely subfigures 15c, 15f and 15i, shows the other elementary functions that compose the reaction rates. On each of these figures are represented $f_R(O) = O/(\mathcal{K}_O + O)$ present in the respiration rate (14b), $f_S(S) = S/(\mathcal{K}_S + S)$ and $f_N(Q) = \max\{Q_{max} - \max\{Q, Q_{min}\}\}/(Q_{max} - Q_{min})$ present in the functional biomass synthesis rate (14c) and $f_D(O) = 1 - \beta\hat{O}/\left(\hat{O}^\beta + \beta - 1\right)$, with $\hat{O} = O/O_{ref}$, present in the death rates (14g) and (14h).

it differs on several points. Apart from the more detailed biological processes, leading to an unusual incompressibility constraint, we considered a third velocity in force balance equations and we added a diffusion term for the components dissolved in liquid.

In addition, we have tailored a numerical scheme, able to deal with the stiffness of the reaction terms. This numerical scheme can be straightforwardly extended in two and three dimensions.

The model involves many parameters, and biological information are lacking to accurately calibrate all of them. Many of them are given in the literature, but some of them remain unknown and have to be calibrated. Consequently, in a further work, sensibility analyses and biological experiments are scheduled in order to set up more precisely the parameters. A careful confrontation of the model in 2D or 3D with experimental results is also foreseen.

The numerical simulations presented are in agreement with the experimental ranges of the literature, especially for daily production rates and front speeds. In these simulations, we can observe that the biofilm is composed of three distinct regions: the front, made of microalgae performing photosynthesis, the middle of the biofilm composed of EPS matrix and microalgae and finally the core where only extra-cellular matrix remains. First results in 2D or 3D show that this biofilm structure is conserved

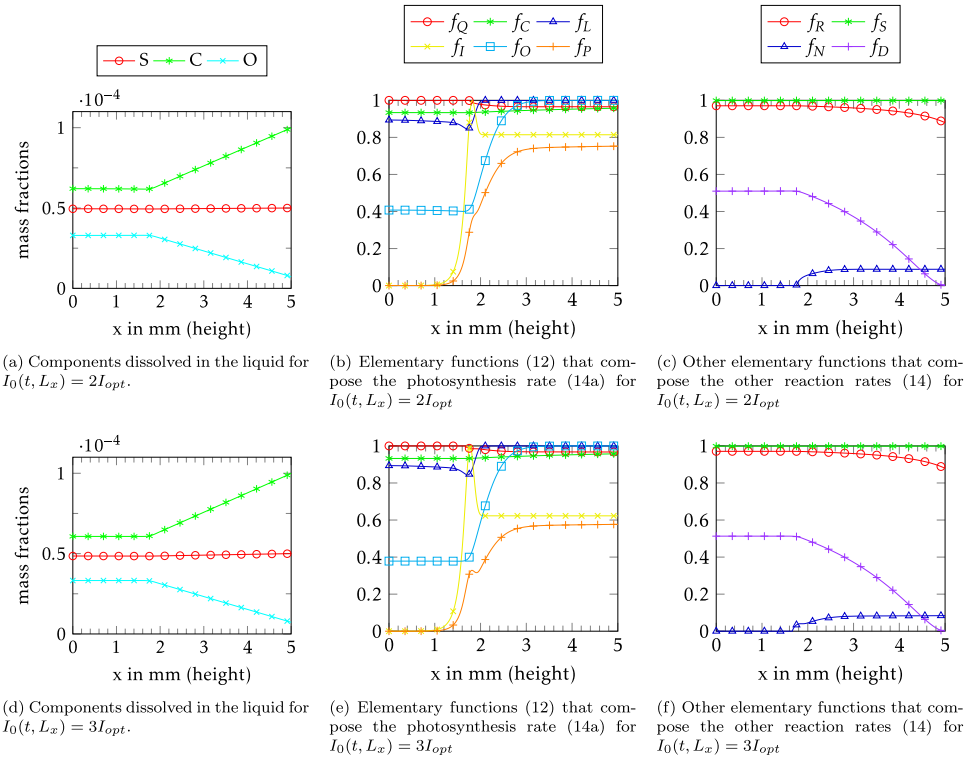

(a) Components dissolved in the liquid for $I_0(t, L_x) = 2I_{opt}$.

(b) Elementary functions (12) that compose the photosynthesis rate (14a) for $I_0(t, L_x) = 2I_{opt}$

(c) Other elementary functions that compose the other reaction rates (14) for $I_0(t, L_x) = 2I_{opt}$

(d) Components dissolved in the liquid for $I_0(t, L_x) = 3I_{opt}$.

(e) Elementary functions (12) that compose the photosynthesis rate (14a) for $I_0(t, L_x) = 3I_{opt}$

(f) Other elementary functions that compose the other reaction rates (14) for $I_0(t, L_x) = 3I_{opt}$

Fig. 16. Influence of variation of light. Numerical results at t=150 days when the biofilm is periodically enlightened. Each row corresponds to a different value for the light intensity on the upper surface: in the first row which corresponds to subfigures 16a, 16b and 16c $I_0(t, L_x) = 0$ and in the second row which corresponds to subfigures 16d, 16e and 16f $I_0(t, L_x) = I_{opt}/2$. The left column, namely subfigures 16a and 16d, shows the mass fractions of the components dissolved in the liquid. On each of these figures are represented the substrate (S, red), the carbon dioxyde (C, green) and the oxygen (O, blue). The middle column, namely subfigures 16b and 16e, shows the functions that compose the photosynthesis rate (14a). On each of these figures are represented $f_Q(Q_{max} - Q_{min})/Q_{max} = \max\{0, 1 - Q_{min}/\min\{Q, Q_{max}\}\}$ in red (12b), $f_C(C) = C/(\mathcal{K}_C + C)$ in green (12c), $f_L(L) = (\mathcal{K}_L + 1)L/(\mathcal{K}_L + L)$ in night blue (12c), $f_I(I) = 2(1 + \mathcal{K}_I)\hat{I}/\left(\hat{I}^2 + 2\mathcal{K}_I\hat{I} + 1\right)$ with $\hat{I} = I/I_{opt}$ in yellow (12e), $f_O(O) = 1/\left(1 + (O/\mathcal{K}_O)^\alpha\right)$ in cyan (12d) and $f_P = f_Q\ f_C\ F_L\ F_I\ f_O(Q_{max} - Q_{min})/Q_{max}$ in orange. The third column, namely subfigures 16c and 16f, shows the other elementary functions that compose the reaction rates. On each of these figures are represented $f_R(O) = O/(\mathcal{K}_O + O)$ present in the respiration rate (14b), $f_S(S) = S/(\mathcal{K}_S + S)$ and $f_N(Q) = \max\{Q_{max} - \max\{Q, Q_{min}\}\}/(Q_{max} - Q_{min})$ present in the functional biomass synthesis rate (14c) and $f_D(O) = 1 - \beta\hat{O}/\left(\hat{O}^\beta + \beta - 1\right)$, with $\hat{O} = O/O_{ref}$, present in the death rates (14g) and (14h).

and that mushroom-shaped structures do appear, as described in Zhang et al. (2008a, b).

However, some hypotheses have been made for simplification purposes and deserve a careful attention. The following suggestions are perspectives for this work. Most of them require preliminary experimental studies to appropriately adapt the kinetics.

First, most of our kinetics on the effects of light and nutrients are derived from models developed for planktonic microalgae. We expect these effects to be also true in biofilms, but complementary experiments are necessary. Second, no limiting effect of temperature has been taken into account, whereas change of temperature will impact the development of microalgae (Ras et al., 2013) and finally the biofilm kinetics. Another interesting improvement would consist in describing the physical properties of the biofilm, through the form of the stress tensor. Dedicated experiments (Galy et al., 2012) are crucial to determine the physical structure of microalgae biofilms. Finally our model is only valid for short period of time and additional phenomena should be included to represent the behaviour in larger times. For example, we have not modelled the detachment which arises during the biofilm development and which significantly affects the biofilm structure. Since the phenomenon of detachment is still not well understood, our model would be of great interest to test several hypotheses on physiological or physical detachment processes.

This first model can be used and extended to more complicated domains than a simple tank: cultivating microalgae biofilms on rotative systems seems very promising (Bernard et al., 2013b; Gross et al., 2015). In this process, the biofilm is periodically immersed and enlightened. It would be of great interest to adapt the model in order to optimize parameters such as light frequency, light intensity or rotating frequency.

Appendix A. Numerical scheme

The aim of this section is to present the numerical scheme we use to discretise the full set of equations described in Subsection 3.5. This scheme follows, for the spatial discretisation, the strategy of Clarelli et al. (2013) derived for a similar model, that is to say some finite-differences scheme derived from relaxation techniques. In this article, the authors dealt with the two following issues: the computation of the velocities in the case of a vanishing phase and the computation of the pressure term. However, we have to face another difficulty here: the mass exchanges between components are non linear and stiff, so we use some explicit-implicit treatment of the source terms of the mass balance equations in order to preserve the non-negativity of the solutions.

We consider the one dimensional domain $\Omega = [0, L_x]$ of width L_x. The extension of the following scheme to the 2D and 3D cases is straightforward, but in this paper we focus our attention on the one dimensional case. We denote by Δx the space step in the x direction and we use a regular grid on Ω, namely the discretisation points $x_i = i\Delta x$, $1 \le i \le N_x$. The kth time step is denoted by Δt_k and the time discretisations are therefore equal to $t^n = \sum_{k=1}^{n} \Delta t_k$.

We begin with rewriting the full system of Subsection 3.5 under the following form:

$$\partial_t U + \partial_x \mathcal{F}(U, W) = \mathbf{\Gamma}(U) + \partial_x\left(M_\delta L \partial_x\left(\frac{U}{L}\right)\right), \tag{A.1a}$$

$$\partial_t W + \partial_x \mathcal{G}(U,W) = \mathcal{G}_{\mathbf{I}}(U,W) + \mathcal{G}_{\mathbf{T}}(U,W) + \mathcal{G}_{\mathbf{P}}(U), \tag{A.1b}$$

$$L = 1 - A - N - E, \tag{A.1c}$$

$$\partial_x((A+N)v_M + Ev_E + Lv_L) = \frac{\Gamma_A + \Gamma_N}{\rho_M} + \frac{\Gamma_E}{\rho_E} + \frac{\Gamma_L}{\rho_L}, \tag{A.1d}$$

that is to say one equation for the mass balances, one equation for the force balances, the volume condition and the incompressibility constraint. Here, U is a vector containing the mass fractions, W is vector containing the three velocity, $\mathcal{F}$ (resp. $\mathcal{G}$) is the flux of vector U (resp. of vector W), M_δ is the diffusion matrix for U, $\mathbf{\Gamma}(U)$ is the mass exchanges source term in the mass balance equations. The source terms in the force balance equations are split into three parts: the pressure part $\mathcal{G}_{\mathbf{P}}(U)$, the interactions term $\mathcal{G}_{\mathbf{I}}(U,W)$ and the mass exchanges term $\mathcal{G}_{\mathbf{T}}(U,W)$, that is to say:

$$U = \begin{pmatrix} A \\ N \\ E \\ SL \\ CL \\ OL \end{pmatrix}, \quad \mathcal{F}(U,W) = \begin{pmatrix} Av_M \\ Nv_M \\ Ev_E \\ SLv_L \\ CLv_L \\ OLv_L \end{pmatrix},$$

$$\mathbf{\Gamma}(U) = \begin{pmatrix} \Gamma_A \cdot \rho_M^{-1} \\ \Gamma_N \cdot \rho_M^{-1} \\ \Gamma_E \cdot \rho_E^{-1} \\ \Gamma_S \cdot \rho_L^{-1} \\ \Gamma_C \cdot \rho_L^{-1} \\ \Gamma_O \cdot \rho_L^{-1} \end{pmatrix},$$

$$M_\delta = \begin{pmatrix} 0 & & & & & & \\ & 0 & & & & & \\ & & 0 & & & & \\ & & & 0 & & & \\ & & & & \delta_S & & \\ & & & & & \delta_C & \\ & & & & & & \delta_O \end{pmatrix},$$

$$W = \begin{pmatrix} (A+N)v_M \\ Ev_E \\ Lv_L \end{pmatrix},$$

$$\mathcal{G}(U,W) = \begin{pmatrix} (A+N)\left(v_M{}^2 + \gamma_M\right) \\ E\left(v_E{}^2 + \gamma_E\right) \\ Lv_L{}^2 \end{pmatrix},$$

$$\mathcal{G}_{\mathbf{P}}(U) = \begin{pmatrix} -(A+N)\partial_x P \\ -E\partial_x P \\ -L\partial_x P \end{pmatrix},$$

$$\mathcal{G}_{\mathbf{I}}(U,W) = \begin{pmatrix} -\frac{m_{ML}}{\rho_M}(v_M - v_L) - \frac{m_{ME}}{\rho_M}(v_M - v_E) \\ -\frac{m_{EL}}{\rho_E}(v_E - v_L) + \frac{m_{ME}}{\rho_E}(v_M - v_E) \\ \frac{m_{ML}}{\rho_L}(v_M - v_L) + \frac{m_{EL}}{\rho_L}(v_E - v_L) \end{pmatrix},$$

$$\mathcal{G}_{\mathbf{T}}(U,W) = \begin{pmatrix} \frac{\Gamma_A + \Gamma_N}{\rho_M} v_M \\ \frac{\Gamma_E}{\rho_E} v_E \\ -\frac{1}{\rho_L}((\Gamma_A + \Gamma_N)v_M + \Gamma_E v_E) \end{pmatrix}.$$

We denote by U_i^n and W_i^n the discrete approximations of $U(t^n, x_i)$ and $W(t^n, x_i)$.

A1. Numerical approximation of mass balance equations

The first step consists in solving Eq. (A.1a), using an explicit discretisation based on a relaxation technique, presented in Aregba-Driollet and Natalini (2000) and used in Clarelli et al. (2013), for the flux term and a mixed strategy for the diffusion term and the source term. More precisely for the diffusion, U is treated implicitly to reduce the CFL condition, whereas L is taken explicitly. The spatial discretisation is done with classical finite differences method which involves numerical approximations of L in the middle of interval $[x_i, x_{i+1}]$; they are interpolated as the mean values of L, namely $L_{i+\frac{1}{2}} = \frac{1}{2}(L_{i+1} + L_i)$. The strategy for the source term is explained further on. We obtain therefore a scheme of the form:

$$U_i^{n+1} - \Delta t \mathbf{\Gamma}\left(U_i^n, U_i^{n+1}\right) - \frac{\Delta t}{\Delta x^2}\left(L_{i+\frac{1}{2}}^n\left(\frac{U_{i+1}^{n+1}}{L_{i+1}^n} - \frac{U_i^{n+1}}{L_i^n}\right)\right.$$
$$\left. - L_{i-\frac{1}{2}}^n\left(\frac{U_i^{n+1}}{L_i^n} - \frac{U_{i-1}^{n+1}}{L_{i-1}^n}\right)\right) = U_i^n - \frac{\Delta t}{2\Delta x}\left(\mathcal{F}\left(W_{i+1}^n\right)\right.$$
$$\left. - \mathcal{F}\left(W_{i-1}^n\right)\right) + \lambda\frac{\Delta t}{4\Delta x}\left(U_{i+1}^n - 2U_i^n + U_{i-1}^n\right),$$

where the numerical velocity λ is common to the mass balance equations and to the force balance equations and is equal to the maximum of the eigenvalues of the Jacobian matrix of the fluxes $\begin{pmatrix} \mathcal{F} \\ \mathcal{G} \end{pmatrix}$, that is to say:

$$\lambda = \max\left\{|2v_L|, |v_M| + \sqrt{\frac{\gamma_M}{\rho_M}}, |v_E| + \sqrt{\frac{\gamma_E}{\rho_E}}\right\}.$$

For stability reasons, the time step Δt is computed at each time step such that the stability condition $\lambda\Delta t \le \Delta x$ is satisfied.

Now, let us explain how to compute the source terms with the explicit - implicit strategy, in order to guarantee that each component of U remains in [0, 1]. From now on in this subsection, we will drop the spatial indices, since no confusion is possible. We therefore discretise, at each point of the domain, the photosynthesis rate, the respiration rate and the functional biomass synthesis rate using implicit expressions for SL, CL and OL at the numerator and explicit expressions for all the other terms, which leads to the following discretisations:

$$\varphi_P(U^n, U^{n+1}) = \mu_A \rho_M N^n\left(1 - \frac{Q_{min}}{Q^n}\right) \times \frac{(CL)^{n+1}}{(\mathcal{K}_L + L^n)(\mathcal{K}_C + C^n)},$$

$$\varphi_R(U^n, U^{n+1}) = \mu_R \rho_M A^n \frac{(OL)^{n+1}}{L^n\mathcal{K}_R + (OL)^n},$$

$$\varphi_N(U^n, U^{n+1}) = \mu_N \rho_M N^n \frac{(SL)^{n+1}}{L^n\mathcal{K}_S + (SL)^n}\frac{Q_{max} - Q^n}{Q_{max} - Q_{min}}.$$

Note that the two other reaction rates, namely the EPS excretion rate and the microalgae death rate, are treated explicitly. The source terms are consequently approximated at each point of the domain by:

$$\Gamma_A\left(U^n, U^{n+1}\right) = \frac{1}{\rho_M}\left(\varphi_P(U^n, U^{n+1}) - \varphi_R(U^n, U^{n+1})\right.$$
$$\left. - \eta_N^A\varphi_N(U^n, U^{n+1}) - \varphi_E^A(U^n) - \varphi_D^A(U^n)\right),$$

$$\Gamma_N\left(U^n, U^{n+1}\right) = \frac{1}{\rho_M}\left(\varphi_N(U^n, U^{n+1}) - \varphi_E^N(U^n)\right.$$
$$\left. - \varphi_D^N(U^n)\right),$$

$$\Gamma_E(U^n) = \frac{1}{\rho_E}\left(\varphi_E^A(U^n) + \varphi_E^N(U^n) + \varphi_D^A(U^n)\right.$$
$$\left. + \varphi_D^N(U^n)\right),$$

$$\Gamma_S\big(U^n,U^{n+1}\big)=-\frac{\eta_N^S}{\rho_L}\varphi_N(U^n,U^{n+1}),$$
$$\Gamma_C\big(U^n,U^{n+1}\big)=\frac{1}{\rho_L}\big(-\eta_P^C\varphi_P(U^n,U^{n+1})+\eta_R^C\varphi_R(U^n,U^{n+1})\big),$$
$$\Gamma_O\big(U^n,U^{n+1}\big)=\frac{1}{\rho_L}\big(\eta_P^O\varphi_P(U^n,U^{n+1})-\eta_R^O\varphi_R(U^n,U^{n+1})\big).$$

In practice, since we do not treat implicitly any variable in the denominator of the source terms, each component of U^{n+1} can be easily computed through the resolution of linear systems. The overall strategy at time step t^{n+1} is the following: we first obtain the volume fractions $(SL)^{n+1}$, $(CL)^{n+1}$ and $(OL)^{n+1}$ as the solutions of linear systems, which allows to compute the reaction rates $\varphi_P(U^n,U^{n+1})$, $\varphi_R(U^n,U^{n+1})$ and $\varphi_N(U^n,U^{n+1})$. It is then straightforward to compute the remaining components of U^{n+1}, that is to say A^{n+1},N^{n+1} and E^{n+1}. Finally, an approximation of the volume fraction of liquid is given thanks to condition (A.1c).

A2. Numerical approximation of force balance equations

Dealing with the computation of force balance equations, we face two difficulties: vanishing phases and computation of the pressure term.

Firstly, force balance equations give the evolution of the momentum of each component, whereas the friction forces depend on the velocities. As a consequence, when one of the phases is vanishing, it is not clear how to define its velocity, that is needed to approximate the friction forces at the following time step. Note that, in a biological context, situations where for example $L=1$ and $A=N=E=0$ are relevant and we cannot claim to be far from vacuum, as can be done in a physical context. Therefore, in order to compute the velocities, we use an implicit-explicit time discretisation strategy for the momentum equations, where the interaction forces term $\mathcal{G}_{\mathbf{I}}(U,W)$ is treated implicitly, see Clarelli et al. (2013).

Secondly, to compute the velocities, we need to know the gradient of the hydrostatic pressure, which is another unknown of the system. A natural approach consists in finding an equation verified by P, by taking the divergence of the sum of the momentum equations and by using Eq. (A.1d). However, this method, which is known to be inefficient, leads to an elliptic equation for P with a non-unique solution. To overcome this difficulty we use a splitting approach which is basically an adaptation of the Chorin-Temam projection method (Chorin, 1968; Temam, 1968), see again Clarelli et al. (2013). This method uses a projection-correction approach: first, we compute an approximation of the velocities using the force balance equations without the pressure terms; then, using the predicted velocities and the average incompressibility constraint, we compute the pressure as the solution of an elliptic equation. Finally, the velocities are corrected thanks to the value of $\partial_x P$.

Let us recall that the vector U^{n+1} is computed at a previous step. We now give some details on the scheme for the force balance equations computation.

First, the projection step enables us to estimate some predicted values $V^{n+\frac{1}{2}}$ for the velocities and this first step of the scheme writes as:

$$\mathcal{M}_i^{n+1}V_i^{n+\frac{1}{2}}=W_i^n-\frac{\Delta t}{2\Delta x}\big(\mathcal{G}(U,W)_{i+1}^n-\mathcal{G}(U,W)_{i-1}^n\big)+\lambda\frac{\Delta t}{4\Delta x}\big(W_{i+1}^n-2W_i^n+W_{i-1}^n\big)+\Delta t\mathcal{G}_{\mathbf{T}}\big(U_i^{n+1},W_i^n\big) \tag{A.2}$$

where

$$V=\begin{pmatrix}v_M\\ v_E\\ v_L\end{pmatrix},$$

$$\mathcal{G}_{\mathbf{T}}\big(U^{n+1},W^n\big)=\begin{pmatrix}\frac{\Gamma_M{}^{n+1}}{\rho_M}v_M{}^n\\ \frac{\Gamma_E{}^{n+1}}{\rho_E}v_E{}^n\\ -\frac{1}{\rho_L}\big(\Gamma_M{}^{n+1}v_M{}^n+\Gamma_E{}^{n+1}v_E{}^n\big)\end{pmatrix},$$

$$\mathcal{M}_i^{n+1}=\begin{pmatrix}\Lambda_1 & -\frac{\Delta t}{\rho_M}m_{ME} & -\frac{\Delta t}{\rho_M}m_{ML}\\ -\frac{\Delta t}{\rho_E}m_{ME} & \Lambda_2 & -\frac{\Delta t}{\rho_E}m_{EL}\\ -\frac{\Delta t}{\rho_L}m_{ML} & -\frac{\Delta t}{\rho_L}m_{EL} & \Lambda_3\end{pmatrix},$$

$$\Lambda_1=A_i^{n+1}+N_i^{n+1}+\frac{\Delta t}{\rho_M}(m_{ML}+m_{ME}),$$
$$\Lambda_2=E_i^{n+1}+\frac{\Delta t}{\rho_E}(m_{EL}+m_{ME}),$$
$$\Lambda_3=L_i^{n+1}+\frac{\Delta t}{\rho_L}(m_{ML}+m_{EL}).$$

Note that the matrix $\mathcal{M}$ contains also the coefficients of the interaction terms, which are treated implicitly, and that this matrix can be computed thanks to the knowledge of U^{n+1}. Moreover, we can compute the determinant of $\mathcal{M}$, namely

$$\det\mathcal{M}=(A+N)EL+\Delta t\Big(\frac{m_{ML}}{\rho_L}(A+N)E+\frac{m_{EL}}{\rho_L}(A+N)E+\frac{m_{EL}}{\rho_E}(A+N)L+\frac{m_{ME}}{\rho_E}(A+N)L+\frac{m_{ML}}{\rho_M}EL+\frac{m_{ME}}{\rho_M}EL\Big)+\Delta t^2\big(m_{EL}m_{ML}+m_{ME}m_{ML}+m_{ME}m_{EL}\big)\Big(\frac{A+N}{\rho_E\rho_L}+\frac{E}{\rho_M\rho_L}+\frac{L}{\rho_M\rho_E}\Big),$$

which is a polynomial of degree 2 in Δt with positive coefficients. Since all the friction coefficients are strictly positive and since the constraint $A+N+E+L=1$, with A, N, E, L positive, is satisfied, the leading coefficient of $\det\mathcal{M}$ is non zero. So, for all Δt strictly positive, $\det\mathcal{M}$ does not vanish and linear system (A.2) has a unique solution.

Then in the second step of splitting we have to solve

$$\partial_t\big(\phi v_\phi\big)=-\frac{\phi}{\rho_\phi}\partial_x P \tag{A.3}$$

for $\phi=M,E,L$ in the interval $[t^n,t^n+\Delta t]$ with initial data $\phi^{n+1}v_\phi^{n+\frac{1}{2}}$. The discrete approximation of these equations for $\phi=M,E,L$ is given by

$$\phi^{n+1}v_\phi^{n+1}-\phi^{n+1}v_\phi^{n+\frac{1}{2}}=-\Delta t\frac{\phi^{n+1}}{\rho_\phi}\partial_x P^{n+1}.$$

Then taking the divergence of the sum of these equations over ϕ we get

$$\partial_x\Big(\big(A^{n+1}+N^{n+1}\big)v_M^{n+1}+E^{n+1}v_E^{n+1}+L^{n+1}v_L^{n+1}\Big)-\partial_x\Big(\big(A^{n+1}+N^{n+1}\big)v_M^{n+\frac{1}{2}}+E^{n+1}v_E^{n+\frac{1}{2}}+L^{n+1}v_L^{n+\frac{1}{2}}\Big)=-\Delta t\partial_x\Big(\Big(\frac{A^{n+1}+N^{n+1}}{\rho_M}+\frac{E^{n+1}}{\rho_E}+\frac{L^{n+1}}{\rho_L}\Big)\times\partial_x P^{n+1}\Big).$$

Now using the discrete approximation of the incompressibility constraint (A.1d), we deduce that P is solution of an elliptic

equation with non constant coefficients:

$$\Delta t\partial_x\left(\left(\frac{\left(A^{n+1}+N^{n+1}\right)}{\rho_M}+\frac{E^{n+1}}{\rho_E}+\frac{L^{n+1}}{\rho_L}\right)\partial_x P^{n+1}\right)= \partial_x\left(\left(A^{n+1}+N^{n+1}\right)v_M^{n+\frac{1}{2}}+E^{n+1}v_E^{n+\frac{1}{2}}+L^{n+1}v_L^{n+\frac{1}{2}}\right) - \frac{\Gamma_A^{n+1}+\Gamma_N^{n+1}}{\rho_M}-\frac{\Gamma_E^{n+1}}{\rho_E}-\frac{\Gamma_L^{n+1}}{\rho_L}. \tag{A.4}$$

This equation is completed with Neumann boundary conditions on P. This boundary condition can be directly deduced from boundary conditions on the velocities and Eq. (A.3) on the boundary defined by $x=0$. For $x=L_x$, we need to note that, in this step, v_T does not change since none of the volume or mass fractions are modified, so using Eq. (A.3) we also get Neumann boundary condition for the pressure on $x=L_x$. However, with Neumann boundary conditions on P, Eq. (A.4) does not have a unique solution. In practice, we choose the solution for which the average value of P is null, that is to say the solution satisfying

$$\int_0^{L_x} P(t,y)\ dy=0.$$

Finally in order to get a symmetric system we rather solve the minimisation problem

$$\Delta t\partial_x\left(\left(\frac{A^{n+1}+N^{n+1}}{\rho_M}+\frac{E^{n+1}}{\rho_E}+\frac{L^{n+1}}{\rho_L}\right)\partial_x P^{n+1}\right)+\lambda= \partial_x\left(\left(A^{n+1}+N^{n+1}\right)v_M^{n+\frac{1}{2}}+E^{n+1}v_E^{n+\frac{1}{2}}+L^{n+1}v_L^{n+\frac{1}{2}}\right) - \frac{\Gamma_A^{n+1}+\Gamma_N^{n+1}}{\rho_M}-\frac{\Gamma_E^{n+1}}{\rho_E}-\frac{\Gamma_L^{n+1}}{\rho_L},$$

$$\int_0^{L_x} P^{n+1}\ dy=0,$$

$$\left(\partial_x P^{n+1}\right)(0)=\left(\partial_x P^{n+1}\right)(L_x)=0,$$

with λ the Lagrange multiplier associated to the constraint $\int_0^{L_x} P^{n+1}\ dy=0$. This system is discretised using classical centered finite differences method and leads to the resolution of a linear symmetric system.

Finally since the volume fractions do not change in this step, we update velocities as follows:

$$v_M^{n+1}=v_M^{n+\frac{1}{2}}-\frac{\Delta t}{\rho_M}(\partial_x P)^{n+1},$$

$$v_E^{n+1}=v_E^{n+\frac{1}{2}}-\frac{\Delta t}{\rho_E}(\partial_x P)^{n+1},$$

$$v_L^{n+1}=v_L^{n+\frac{1}{2}}-\frac{\Delta t}{\rho_L}(\partial_x P)^{n+1}.$$

Appendix B. Numerical simulations

B1. Influence of the values of elastic interaction tensor coefficients γ_M and γ_E

According to Clarelli et al. (2013), the value of the elastic tensor coefficient γ drives the speed of the biofilm front. In our model, unlike in Clarelli et al. (2013), we consider two distinct elastic tensor coefficients: γ_M for microalgae and γ_E for extra-cellular matrix. In Section 4.1, simulations were performed with $\gamma_M=\gamma_E$; however, in Figs. B1 and B2, we show the volume and mass fractions and the velocities obtained for $\gamma_M=1.5\cdot10^{-7}$ kg m^{-1}d^{-2} and $\gamma_E=5\cdot10^{-8}$ kg m^{-1}d^{-2}. The values of the volume fractions and the composition of the biofilm are the same as in Section 4.1, with a difference of less than 7%. However, the velocity of extracellular matrix is lower than the microalgae velocity in this case.

Note that when $\gamma_E\geq\gamma_M$, the conclusion is similar: the composition of the biofilm does not change and the velocity of extracellular matrix is greater than the microalgae velocity. In practice, the influence of γ_E appears to be low, unlike γ_M that drives the velocity of the biofilm front.

As in Clarelli et al. (2013), we can observe in Fig. B3(a) that the front velocity depends linearly on $\sqrt{\gamma_M}$. Indeed, the front velocity determined with numerical experiments (red marks) fits the linear regression (in blue) given by $y=5.6524\cdot10^{-2}x+4.9844\cdot10^{-6}$ with correlation coefficient equal to 0.9994. In Fig. B3(b) we represent the average daily production rate (defined as the difference of dry biomass between two consecutive days) of dry biomass over 90 days. Again we observe that numerical experiments (red marks) fit the linear regression (in blue) given by $y=868.12x+0.81629$ with correlation coefficient equal to 0.996.

B2. Influence of maximal photosynthesis rate

In this subsection, we investigate the influence of maximal photosynthesis rate μ_P.

Fig. B4(a) represents the average daily production rate (estimated on 90 days) of dry biomass for the different constituents of the biofilm with respect to maximal photosynthesis rate μ_P. As it can be expected, the production rate of pool of carbon storage increases with the value of the maximal photosynthesis rate. Since all other biofilm components (**N** and **E**) are synthesised from carbohydrates of the pool of carbon storage, their production rates also increase with the maximal photosynthesis. So the growth of the whole biofilm (**A, N** and **E**) increases with μ_P. Consequently, the velocity of the front, which is represented on Fig. B4(b), also rises with the maximal photosynthesis rate.

However, the production rates and the velocity of the biofilm front increase more slowly when μ_P increases, meaning that biofilm growth is limited. Indeed, as μ_P increases, the photosynthesis rate rises and also leads to an increase of oxygen released by this mechanism. So, the oxygen mass fraction near the biofilm front becomes very high and inhibits increasingly the photosynthesis rate.

Appendix C. Parameters estimation

C1. Estimation of the stoichiometric coefficients

Photosynthesis can be resumed by

$$6CO_2+6H_2O\longrightarrow C_6H_{12}O_6+6O_2.$$

Moreover glucose ($C_6H_{12}O_6$) is part of the pool of carbon storage **A**. By definition, mass of the latter is composed of 90% of water. So the mechanism of photosynthesis, in terms of considered components, writes as

$$\begin{array}{ccc}\eta_P^C\mathbf{C}+\eta_P^L\mathbf{L} & \longrightarrow & \eta_P^A\mathbf{A}+\eta_P^O\mathbf{O}\\ 6CO_2+96H_2O & \longrightarrow & C_6H_{12}O_6+90H_2O+6O_2.\end{array}$$

Then using the molar mass of each component we easily deduce the stoichiometric coefficients.

Since respiration can be summarised as the reverse chemical reaction, the estimation of the stoichiometric coefficients can be directly deduce from the coefficients obtained for photosynthesis.

Neglecting secondary reactants and products, the functional biomass synthesis is

$$1.31NO_3+1.14C_6H_{13}O_9S_1\longrightarrow C_{8.59}H_{14.13}O_{2.49}N_{1.26}P_{0.15}S_{0.025},$$

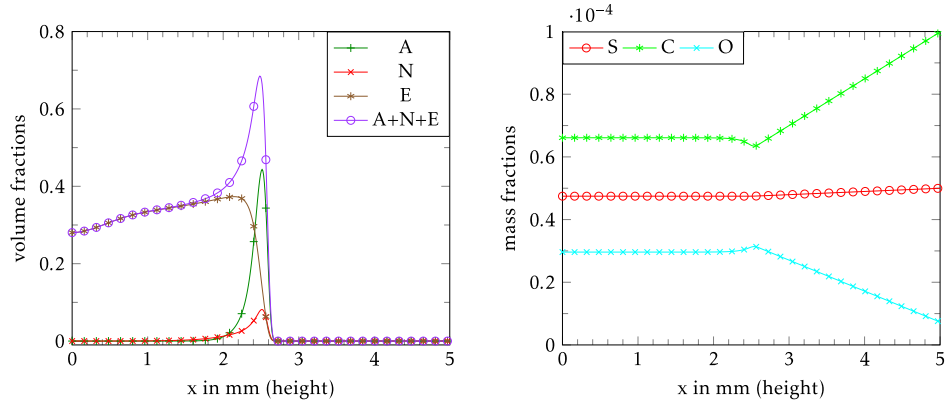

(a) Volume fraction of the different biofilm constituents with respect to height at $t = 90$ days when the value of the elastic tensor is changed to $\gamma_E = 5 \cdot 10^{-8}$ kg m^{-1} d^{-2}. This figure shows the pool of carbon storage (A, green), the functional biomass (N, red), the extra-cellular matrix (E, brown) and the whole biofilm (A+N+E, purple).

(b) Mass fraction of the different components dissolved in the liquid with respect to height at $t = 90$ days when the value of the elastic tensor is changed to $\gamma_E = 5 \cdot 10^{-8}$ kg m^{-1} d^{-2}. This figure shows the substrate (S, red), the carbon dioxyde (C, green) and the oxygen (O, blue).

Fig. B1. Influence of the values of elastic interaction tensor coefficients. Composition of biofilm does not change and the velocity of extra-cellular matrix is greater than the microalgae velocity. Plot of volume fraction of the biofilm components in subfigure 17a (left), and mass fraction of the components dissolved in the liquid in subfigures 17b (right), with respect to height at t=90 days and when the value of the elastic tensor coefficient for extra-cellular matrix is changed to $\gamma_E = 5 \cdot 10^{-8}$ kg m^{-1}d^{-2}.

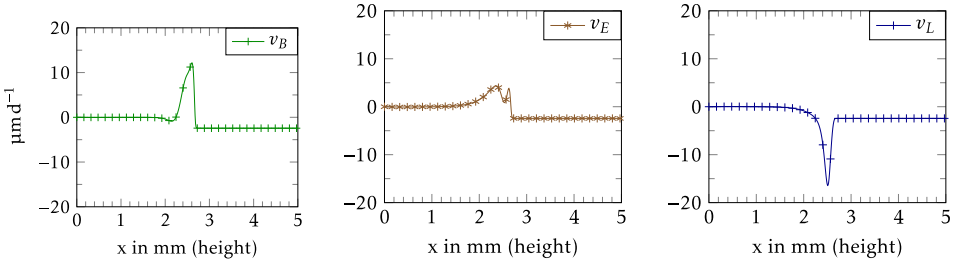

(a) Microalgae velocity (v_M)

(b) Extra-cellular matrix velocity (v_E)

(c) Liquid velocity (v_L)

Fig. B2. Influence of the values of elastic interaction tensor coefficients. Composition of biofilm does not change and the velocity of extra-cellular matrix is greater than the microalgae velocity. Plot of velocities of the different components of the system with respect to height at $t = 90$ days when the value of the elastic tensor coefficient for extra-cellular matrix is changed to $\gamma_E = 5 \cdot 10^{-8}$ kg m^{-1}d^{-2}. Subfigure 18a on the left represents the velocity v_M of the microalgae (carbon pool and functional biomass), subfigure 18b in the middle represents the velocity v_E of the extra-cellular matrix and subfigure 18c on the right represents the velocity v_L of the liquid.

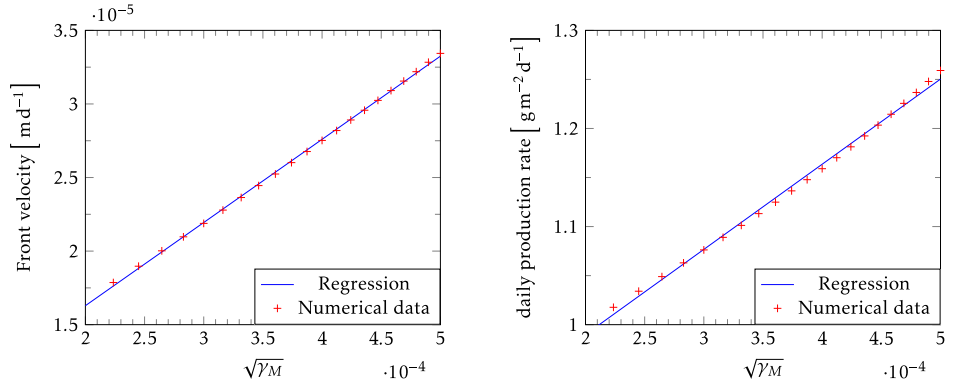

(a) Numerical estimate and linear approximation, over 90 day, of the averaged velocity of the biofilm front, with respect to the square root of the elastic tensor coefficient for the biofilm constituents $\sqrt{\gamma_M} = \sqrt{\gamma_E}$.

(b) Numerical estimate and linear approximation, over 90 days, of the daily production rate of dry biomass, with respect to the square root of the elastic tensor coefficient for the biofilm constituents $\sqrt{\gamma_M} = \sqrt{\gamma_E}$.

Fig. B3. Influence of the values of elastic interaction tensor coefficients. Front velocity depends linearly on $\sqrt{\gamma_M}$. Numerical estimate and linear approximation, over 90 days of the average velocity of the biofilm front in subfigure 19a and of the daily production rate of dry biomass in subfigure 19b with respect to the elastic tensor coefficient for the biofilm constituents $\sqrt{\gamma_M} = \sqrt{\gamma_E}$.

according to Baroukh et al. (2014, Table 1). Then, considering that the functional biomass and the pool of carbon storage contains 90% of liquid and using the molar mass of each component, we easily deduce the stoichiometric coefficients η_N^A and η_N^S.

C2. Estimation of the EPS excretion rates

According to Xiao and Zheng (2016, Table 3), microalgae EPS contains between 1% and 16.9% of proteins. Denoting π the percentage of proteins in the EPS we have that $\max \varphi_E^N = \pi \max \varphi_E^A$.

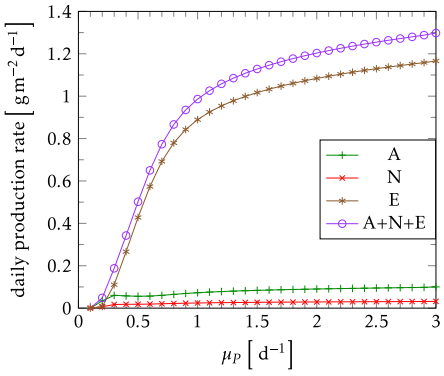

(a) Average production rate of biofilm constituent during 90 days with respect to the maximal photosynthesis rate. In this figure we display the production rate of carbon pool (A, green), functional biomass (N, red), extra-cellular matrix (E, brown) and of the whole biofilm (A+N+E, purple).

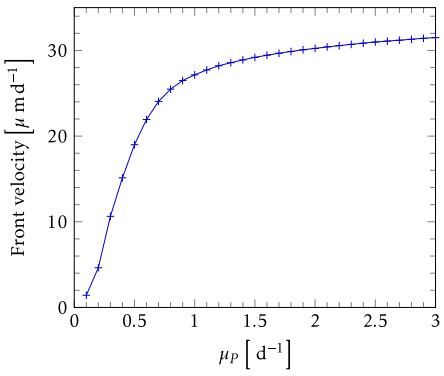

(b) Average velocity of the biofilm front during 90 days with respect to the maximal photosynthesis rate.

Fig. B4. Influence of maximal photosynthesis rate. Production rate of pool of carbon storage increases with the value of the maximal photosynthesis rate. Plot of the average daily production rate of biofilms constituents in subfigure 20a and of the average velocity of the biofilm front in subfigure 20b during 90 days.

Then using the definition of the internal functional biomass quota Q, we deduce that

$$\mu_E^N = \pi \mu_E^A \frac{Q_{max}}{1 - Q_{max}}, \tag{C.1}$$

which leads to $\mu_E^N \in [0.016, 0.27]$.

C3. Estimation of ρ_E

Without experimental knowledge, we assume that EPS density is of the same order of magnitude as microalgae density, and thus we set $\rho_E = \rho_M$.

C4. Estimation of the mortality parameters: $\mathcal{K}_D$ *and* β

By definition of the mortality rate f_D, $\mathcal{K}_D$ is the oxygen saturation for which the mortality rate is minimal. We assume the value of $\mathcal{K}_D$ is the oxygen saturation at equilibrium without microalgae, namely there is no death induced by oxygen if $O = \theta_O$. Thus according to Rubio et al. (1999), we set $\mathcal{K}_D = 7.2 \cdot 10^{-6}$ kg**O**/kg**L**.

We assume that the death is triggered for the same oxygen saturation that the photosynthesis inhibition. Thus, we estimate β by solving $f_D(\mathcal{K}_O/\mathcal{K}_D) = 1/2$.

References

Alpkvist, E., Klapper, I., 2007. A multidimensional multispecies continuum model for heterogeneous biofilm development. Bull. Math. Biol. 69 (2), 765–789.

Alpkvist, E., Picioreanu, C., van Loosdrecht, M.C., Heyden, A., 2006. Three-dimensional biofilm model with individual cells and continuum EPS matrix. Biotechnol. Bioeng. 94 (5), 961–979.

Ambrosi, D., Preziosi, L., 2002. On the closure of mass balance models for tumor growth. Math. Models Methods Appl. Sci. 12 (5), 737–754.

Andrews, J.F., 1968. A mathematical model for the continuous culture of microorganisms utilizing inhibitory substrates. Biotechnol. Bioeng. 10 (6), 707–723.

Aregba-Driollet, D., Natalini, R., 2000. Discrete kinetic schemes for multidimensional systems of conservation laws. SIAM J. Numer. Anal. 37 (6), 1973–2004.

Baroukh, C., Muñoz Tamayo, R., Steyer, J.-P., Bernard, O., 2014. A new framework for metabolic modeling under non-balanced growth. application to the carbon metabolism of unicellular microalgae. PLoS ONE 9 (8), 1–15.

Bernard, O., 2011. Hurdles and challenges for modelling and control of microalgae for CO_2 mitigation and biofuel production. J. Process Control 21 (10), 1378–1389.

Bernard, O., Bastin, G., 2005. On the estimation of the pseudo-stoichiometric matrix for macroscopic mass balance modelling of biotechnological processes. Math. Biosci. 193 (1), 51–77.

Bernard, O., Boulanger, A.-C., Bristeau, M.-O., Sainte-Marie, J., 2013. A 2d model for hydrodynamics and biology coupling applied to algae growth simulations. ESAIM: Mathematical Modelling and Numerical Analysis 47 (5), 1387–1412.

Bernard, O., Gouzé, J.-L., 1995. Transient behavior of biological loop models with application to the droop model. Math. Biosci. 127 (1), 19–43.

Bernard, O., Sciandra, A., Pruvost, E., Lopes, F., 2013b. Procédé et installation de production de micro-algues.

Bianchini, R., Natalini, R., 2016. Global existence and asymptotic stability of smooth solutions to a fluid dynamics model of biofilms in one space dimension. J. Math. Anal. Appl. 434 (2), 1909–1923.

Bougaran, G., Bernard, O., Sciandra, A., 2010. Modeling continuous cultures of microalgae colimited by nitrogen and phosphorus. J. Theor. Biol. 265 (3), 443–454.

Chorin, A.J., 1968. Numerical solution of the Navier-Stokes equations. Math. Comp. 22, 745–762.

Clarelli, F., Russo, C.D., Natalini, R., Ribot, M., 2013. A fluid dynamics model of the growth of phototrophic biofilms. J. Math. Biol. 66 (7), 1387–1408.

Clarelli, F., Russo, C.D., Natalini, R., Ribot, M., 2016. A fluid dynamics multidimensional model of biofilm growth: stability, influence of environment and sensitivity. Math. Med. Biol. 33 (4), 371–395.

Costache, T., Fernández, F.A., Morales, M., Fernández-Sevilla, J., Stamatin, I., Molina, E., 2013. Comprehensive model of microalgae photosynthesis rate as a function of culture conditions in photobioreactors. Appl. Microbiol. Biotechnol. 97 (17), 7627–7637.

Costerton, J., Geesey, G., Cheng, K., 1978. How bacteria stick. Scientific American.

Dockery, J., Klapper, I., 2001/02. Finger formation in biofilm layers. SIAM J. Appl. Math. 62 (3), 853–869.

Droop, M.R., 1968. Vitamin B12 and Marine Ecology. IV. the Kinetics of Uptake, Growth and Inhibition in Monochrysis Lutheri. J. Marine Biol. Assoc. United Kingdom 48, 689–733.

Edmundson, S.J., Huesemann, M.H., 2015. The dark side of algae cultivation: characterizing night biomass loss in three photosynthetic algae, chlorella sorokiniana, nannochloropsis salina and picochlorum sp.. Algal. Res. 12, 470–476.

Eilers, P., Peeters, J., 1993. Dynamic behaviour of a model for photosynthesis and photoinhibition. Ecol. Modell. 69 (1), 113–133.

Galy, O., Latour-Lambert, P., Zrelli, K., Ghigo, J.-M., Beloin, C., Henry, N., 2012. Mapping of bacterial biofilm local mechanics by magnetic microparticle actuation. Biophys. J. 103 (6), 1400–1408.

Gross, M., Henry, W., Michael, C., Wen, Z., 2013. Development of a rotating algal biofilm growth system for attached microalgae growth with in situ biomass harvest. Bioresour. Technol. 150, 195–201.

Gross, M., Jarboe, D., Wen, Z., 2015. Biofilm-based algal cultivation systems. Appl. Microbiol. Biotechnol. 99 (14), 5781–5789.

Gudin, C., Chaumont, D., 1991. Cell fragility — the key problem of microalgae mass production in closed photobioreactors. Bioresour. Technol. 38 (2), 145–151.

Henze, M., Grady, C., Gujer, W., Marais, G., Matsuo, T., 1987. A general model for single-sludge wastewater treatment systems. Water Res. 21 (5), 505–515.

Horn, H., Lackner, S., 2014. Productive Biofilms. Springer International Publishing, Cham, pp. 53–76.

Kjellerup, B., Kjeldsen, K.U., Lopes, F., Abildgaard, L., Ingvorsen, K., Frolund, B., Sowers, K.R., Nielsen, P.H., 2009. Biocorrosion and biofilm formation in a nutrient limited heating system subjected to alternating microaerophilic conditions. Biofouling 25 (8), 727–737.

Lange, O.L., Meyer, A., Budel, B., 1994. Net photosynthesis activation of a desiccated cyano-bacterium without liquid water in high air humidity alone. experiments with microcoleus sociatus isolated from a desert soil crust. Funct. Ecol. 8 (1), 52–57.

Lemesle, V., Mailleret, L., 2008. A mechanistic investigation of the algae growth "Droop" model. Acta Biotheor. 56 (1), 87–102.

van Loosdrecht, M., Heijnen, J., Eberl, H., Kreft, J., Picioreanu, C., 2002. Mathematical modelling of biofilm structures. Antonie van Leeuwenhoek 81 (1), 245–256.

Mairet, F., Bernard, O., Masci, P., Lacour, T., Sciandra, A., 2011. Modelling neutral lipid production by the microalga isochrysis aff. galbana under nitrogen limitation. Bioresour. Technol. 102 (1), 142–149. Special Issue: Biofuels - II: Algal Biofuels and Microbial Fuel Cells

Monod, J., 1949. The growth of bacterial cultures. Annu. Rev. Microbiol. 3, 371–394.

Novak, J.T., Brune, D.E., 1985. Inorganic carbon limited growth kinetics of some freshwater algae. Water Res. 19 (2), 215–225.

Peng, L., Lan, C.Q., Zhang, Z., 2013. Evolution, detrimental effects, and removal of oxygen in microalga cultures: a review. Environ. Progress Sust. Energy 32 (4), 982–988.

Rajagopal, K., Tao, L., 1995. Mechanics of mixtures. Series on Advances in Mathematics for Applied Sciences. World Scientific, Singapore.

Ras, M., Steyer, J.-P., Bernard, O., 2013. Temperature effect on microalgae: a crucial factor for outdoor production. Rev. Environ. Sci.Biotechnol. 12 (2), 153–164.

Rubio, F.C., Fernández, F.G.A., Pérez, J.A.S., Camacho, F.G., Grima, E.M., 1999. Prediction of dissolved oxygen and carbon dioxide concentration profiles in tubular photobioreactors for microalgal culture. Biotechnol. Bioeng. 62 (1), 71–86.

Schnurr, P.J., Allen, D.G., 2015. Factors affecting algae biofilm growth and lipid production: a review. Renewable Sustainable Energy Rev. 52, 418–429.

Schnurr, P.J., Espie, G.S., Allen, D.G., 2014. The effect of light direction and suspended cell concentrations on algal biofilm growth rates. Appl. Microbiol. Biotechnol. 98 (20), 8553–8562.

Serra-Maia, R., Bernard, O., Gonçalves, A., Bensalem, S., Lopes, F., 2016. Influence of temperature on chlorella vulgaris growth and mortality rates in a photobioreactor. Algal. Res. 18, 352–359.

Sohm, J.A., Edwards, B.R., Wilson, B.G., Webb, E.A., 2011. Constitutive extracellular polysaccharide (EPS) production by specific isolates of Crocosphaera watsonii. Front. Microbiol. 2, 229.

Staats, N., Stal, L.J., Mur, L.R., 2000. Exopolysaccharide production by the epipelic diatom cylindrotheca closterium: effects of nutrient conditions. J. Exp. Mar. Biol. Ecol. 249 (1), 13–27.

Stomp, M., Huisman, J., Stal, L. J., Matthijs, H. C. P.,. Colorful niches of phototrophic microorganisms shaped by vibrations of the water molecule. ISME J.

Temam, R., 1968. Une méthode d'approximation de la solution des équations de Navier-Stokes. Bulletin de la Société Mathématique de France 96, 115–152.

Thébault, J., Rabouille, S., 2003. Comparison between two mathematical formulations of the phytoplankton specific growth rate as a function of light and temperature, in two simulation models. Ecol. Modell. 163 (1–2), 145–151.

Truesdell, C., Rajagopal, K.R., 1999. An Introduction to the Mechanics of Fluids. Birkhaüser.

Wang, Q., Zhang, T., 2010. Review of mathematical models for biofilms. Solid State. Commun. 150 (21–22), 1009–1022. 0038–1098, Nanoscale Interfacial Phenomena in Complex Fluids

Wijffels, R.H., Barbosa, M.J., 2010. An outlook on microalgal biofuels. Science 329 (5993), 796–799.

Wolf, G., Picioreanu, C., van Loosdrecht, M.C., 2007. Kinetic modeling of phototrophic biofilms: the PHOBIA model. Biotechnol. Bioeng. 97 (5), 1064–1079.

Xiao, R., Zheng, Y., 2016. Overview of microalgal extracellular polymeric substances (EPS) and their applications. Biotechnol. Adv. 34 (7), 1225–1244.

Zeebe, R.E., 2011. On the molecular diffusion coefficients of dissolved , and and their dependence on isotopic mass. Geochim. Cosmochim. Acta 75 (9), 2483–2498.

Zhang, T., Cogan, N., Wang, Q., 2008a. Phase field models for biofilms. i. theory and one-dimensional simulations. SIAM J. Appl. Math. 69 (3), 641–669.

Zhang, T., Cogan, N., Wang, Q., 2008b. Phase-field models for biofilms II. 2-d numerical simulations of biofilm-flow interaction. Commun. Comput. Phys. 4, 72–101.

Zippel, B., Rijstenbil, J., Neu, T.R., 2007. A flow-lane incubator for studying freshwater and marine phototrophic biofilms. J. Microbiol. Methods 70 (2), 336–345.